## RESEARCH ARTICLE

**Key Points:**
- Two-way nested experiment of the Southwest Atlantic circulation
- Evaluate the sensitivity of the circulation to the wind/bottom stress forcings
- Describe the seasonal variability of the SW Atlantic

**Correspondence to:**
V. Combes,
vcombes@coas.oregonstate.edu

# A two-way nested simulation of the oceanic circulation in the Southwestern Atlantic

**Vincent Combes[1] and Ricardo P. Matano[1]**

[1]College of Earth, Ocean and Atmospheric Sciences, Oregon State University, Corvallis, Oregon, USA

**Abstract** This article presents the results of a high-resolution (1/12°), two-way nested simulation of the oceanic circulation in the southwestern Atlantic region. A comparison between the model results and extant observations indicates that the nested model has skill in reproducing the best-known aspects of the regional circulation, e.g., the volume transport of the ACC, the latitudinal position of the BMC, the shelf break upwelling of Patagonia, and the Zapiola Anticyclone. Sensitivity experiments indicate that the bottom stress parameterization significantly impacts the mean location of the Brazil/Malvinas Confluence and the transport of the Zapiola Anticyclone. The transport of the Brazil Current strengthens during the austral summer and weakens during the austral winter. These variations are driven by the wind stress curl over the southwestern Atlantic. The variations of the transport of the Malvinas Current are out of phase with those of the Brazil Current. Most of the seasonal variability of this current is concentrated in the offshore portion of the jet, the inshore portion has a weak seasonality that modulates the magnitude of the Patagonian shelf break upwelling. Using passive tracers we show that most of the entrainment of deep waters into the shelf occurs in the southernmost portion of the Patagonian shelf and along the inshore boundary of the Brazil Current. Shelf waters are preferentially detrained near the Brazil/Malvinas Confluence. Consistent with previous studies, our simulation also shows that south of ∼42°S the Malvinas Current is composed of two jets, which merge near 42°S to form a single jet farther north.

## 1. Introduction

The southwestern Atlantic extends from the tip of Tierra del Fuego, Argentina to Cabo Frio, Brazil (∼22°S) and from the eastern shores of South America to ∼40°W, thus encompassing the shelf and the deep-ocean portions of one of the most energetic and biologically productive oceanic regions of the southern hemisphere. The deep-ocean circulation in this region is characterized by the poleward flow of the warm and salty Brazil Current (BC) in the north and the equatorward flow of the cold and relatively fresh Malvinas Current (MC) in the south (Figure 1). The two western boundary currents meet near 38°S generating a highly energetic region known as the Brazil/Malvinas Confluence (BMC), which is characterized by the continuous formation of warm and cold core eddies and filaments [*Garzoli and Garraffo*, 1989]. The oceanic circulation over the shelf region reflects the deep-ocean patterns with a northeastward flow in the south and a southwestward flow in the north [*Palma et al.*, 2008]. The two flows meet near 33°S forming a density compensated front, the Subtropical Shelf Front that appears as an extension of the BMC over the shelf [*Piola et al.*, 2000]. The shelf circulation reflects the influence of the MC and the BC but it is also modulated by strong winds, high tides, and substantial freshwater discharges from the Magellan Strait and the La Plata River [*Palma et al.*, 2008; *Matano et al.*, 2010; *Auad and Martos*, 2012].

Numerical studies of the southwestern Atlantic shelf circulation have been hampered by the difficulty of solving simultaneously the long spatial and temporal scales associated with the deep-ocean circulation and the relatively short scales associated with the shelf circulation. Thus, modeling efforts aimed to understand the dynamics of the deep-ocean circulation lacked the spatial resolution to represent the shelf circulation [*Matano*, 1993; *Matano et al.*, 1993; *Smith et al.*, 1994; *De Miranda et al.*, 1999; *Barnier et al.*, 2006; *Treguier et al.*, 2001; *Wainer et al.*, 2000; *Fetter and Matano*, 2008], while efforts to understand the shelf circulation lacked the spatial extent to properly represent the deep-ocean circulation [*Glorioso and Flather*, 1995; *Palma et al.*, 2004; *Campos et al.*, 2000; *Castelao et al.*, 2004; *Calado et al.*, 2010; *Palma et al.*, 2008; *Auad and Martos*, 2012]. To advance our understanding of the southwestern Atlantic shelf circulation, we build over previous work and present the results of new simulations in which a high-resolution model of the southwestern Atlantic region is nested into a coarser, but still eddy permitting, model of the entire southern hemisphere
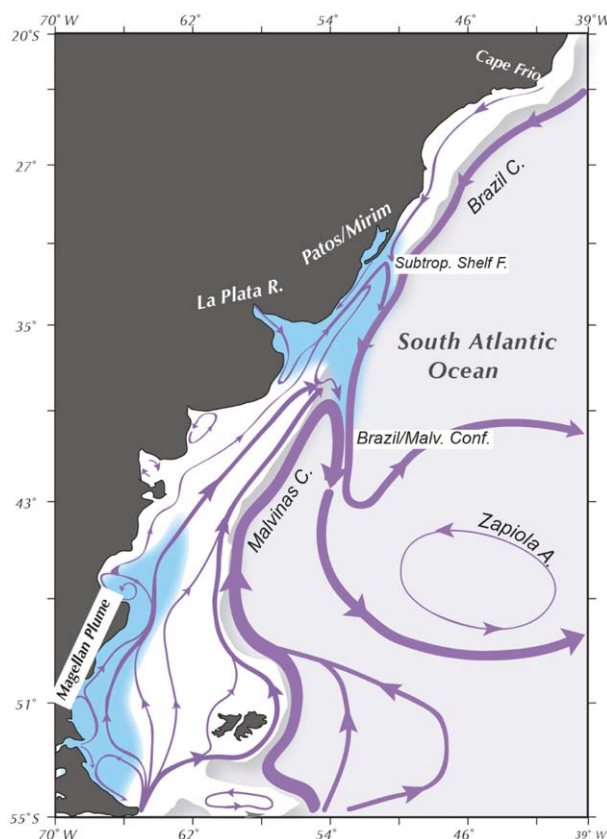
**Figure 1.** Schematic oceanic circulation of the Southwestern Atlantic. Blue regions illustrate the Magellan and La Plata low-salinity plumes. The white (light gray) region indicates the shelf (deep ocean) region.

circulation. This model configuration permits the simultaneous solution of the large-scale processes associated with the deep-ocean circulation and the short-scale processes associated with the shelf circulation. In this article, we describe the model setup, analyze the sensitivity of the regional circulation to model parameterization, and characterize the seasonal variability of the region and the processes controlling the exchanges between the shelf and the deep ocean. In a forthcoming article, we will present a detailed discussion of the shelf circulation including its sensitivity to variations of the atmospheric forcing, tidal forcing, the BC and MC transports and the freshwater inputs.

This article is organized as follows; section 2 describes the model setup. Section 3 describes the control run, which is the benchmark that will be used in our sensitivity studies. Section 4 discusses a set of sensitivity experiments that explore the role of the surface and bottom forcings on the deep-ocean circulation. Section 4.1 compares three experiments forced by seasonal climatology of ERA_Interim (reanalysis produced by the European Centre for Medium-Range Weather Forecasts), NCEP/NCAR (National Centers for Environmental Prediction/National Center for Atmospheric Research), and QuickSCAT (Quick Scatterometer) wind stress. An experiment with weaker bottom stress is performed and analyze in section 4.2 The most realistic configuration derived from section 4 will then be used on sections 5–7 to examine, respectively, the seasonal cycle of the southwestern Atlantic circulation, the Patagonian shelf break upwelling, and the exchanges between the deep ocean and shelf circulations. Section 8 is left for conclusion.

## 2. Model Setup

### 2.1. Model Description

The model used in this study is the Regional Ocean Modeling System (ROMS), which is a three-dimensional, free surface, hydrostatic, eddy-resolving primitive equation ocean model. ROMS uses orthogonal curvilinear coordinates in the horizontal and sigma, terrain following coordinates in the vertical [*Shchepetkin and McWilliams*, 2005]. We use the version ROMS_AGRIF (http://roms.mpl.ird.fr/), which offers the capability of a two-way nesting procedure with a high-resolution "child" model embedded into a coarser resolution "parent" model (Table 1).

### 2.2. Model *Grids*

The parent grid extends 360° in the longitudinal direction and from Antarctica to 15.2° N. It has a spatial resolution of 1/4°, which is ~23 km at the latitude of Buenos Aires (34°S), and 40 sigma levels in the vertical with enhanced resolution at the surface. The child grid extends from 82°W to 41°W and from 64°S to 20°S, thus covering the southern portion of South America and it has a spatial resolution of 1/12°. In the nesting procedure, the parent model is integrated forward by one time step after which it provides the boundary

**Table 1.** Table of Model Control Run Experiment (Exp_CTRL)[a]

| | Spatial Resolution | Run Length (Year) | Surface Forcing | | Initial Condition | Boundary Condition | Tides | Bottom Stress |
|---|---|---|---|---|---|---|---|---|
| | | | Fluxes | Wind | | | | |
| Spinup Southern Hemisphere | 1/4° × 1/4° | 10 | COADS heat and freshwater fluxes | Seasonal Climatology | From OFES | North—From OFES East West—Periodicity | No | αquad = 0.007 |
| EXP_CTRL two ways nesting | Southern Hemisphere | 1/4° × 1/4° | 7 (spinup) + 7 | | ERA_Interim | From Spinup | North—From OFES | Yes (M2 harmonic) | |
| | South America | 1/12° × 1/12° | | | | | Two-ways nesting | | |
| EXP_QSCAT | | | | QSCAT | | | | |
| EXP_NCEP | | | | NCEP/NCAR | | | | |
| EXP_r3 | | | | | | | | αquad = 0.003 |
| EXP_SEASON | | | | | | | | αquad = 0.0045 |

[a]Only the differences from EXP_CTRL are shown for EXP_QSCAT, EXP_NCEP, EXP_r3, and EXP_SEASON.

conditions for the child model, which is integrated forward whence it updates the parent model, and repeats the process. Volume and properties fluxes are conserved at the interface between the parent and the child grids. A detailed description of ROMS architecture can be found in *Debreu et al.* [2011].

### 2.3. Bottom Topography and Freshwater Discharges

The bottom topography was derived from the ETOPO1 (1′ resolution) [*Amante and Eakins*, 2009], which was smoothed to minimize the pressure gradient errors associated with terrain following coordinates [*Mellor et al.*, 1994]. The model includes a 23,000 $m^3 s^{-1}$ discharge from La Plata River (∼34.4°S) and an open channel of constant depth (100 m), connecting the South Pacific to the Patagonian shelf at 70°W–53°S to represent the Magellan Strait. The depth of 100 m has been chosen such that the model outflow (∼100,000 $m^3 s^{-1}$) is close to the estimated value of 85,000 $m^3 s^{-1}$ from the high-resolution simulation of *Sassi and Palma* [2006].

### 2.4. Wind Stress Forcing

We present a suite of simulations that have been forced with monthly climatological mean fields from the ERA-Interim data set, which covers the period 1979–2011 and has a spatial resolution of 0.75° [*Dee et al.*, 2011], the NCEP/NCAR reanalysis data, which extends from 1948 to present and has a 2° spatial resolution [*Kalnay et al.*, 1996], and the QuickSCAT data, which extends from 1999 to 2009 and has a 0.125° spatial resolution [*Lungu*, 2001]. The differences among the three climatologies are largest near the coastal regions (Figure 2). The ERA_Interim and the NCEP/NCAR show stronger zonal wind stress over the southern portion of Patagonia than those indicated by QuickSCAT. The largest differences, however, correspond to the meridional component of the wind stress. The coarse horizontal resolution of the NCEP/NCAR produces stronger zonal wind stress over the southern Patagonian shelf NCEP/NCAR data set than the QuickSCAT winds. Around Antarctica where QuickSCAT data are not available (sea-ice coverage; white regions in Figure 2), the QSCAT surface wind stress is replaced by the ERA_Interim wind stress. We did a set of sensitivity experiments using the three climatologies to assess the sensitivity of the ocean circulation in the southwestern Atlantic to the wind forcing (section 4).

### 2.5. Buoyancy Forcing

All the simulations were forced with heat and freshwater fluxes derived from the Comprehensive Ocean-Atmosphere Data Set (COADS) [*Da Silva et al.*, 1994]. The heat flux also includes a tendency restoring term to the Pathfinder SST climatology. Thus,

$$Q_{modified} = Q_{COADS} + \frac{dQdSST}{\rho C_p} [SST_{model} - SST_{pathfinder}]$$

where $Q_{COADS}$ is the heat flux from the COADS climatology, dQdSST is the kinetic surface net heat flux sensitivity to the SST defined as:

**zonal** wind stress



**meridional** wind stress
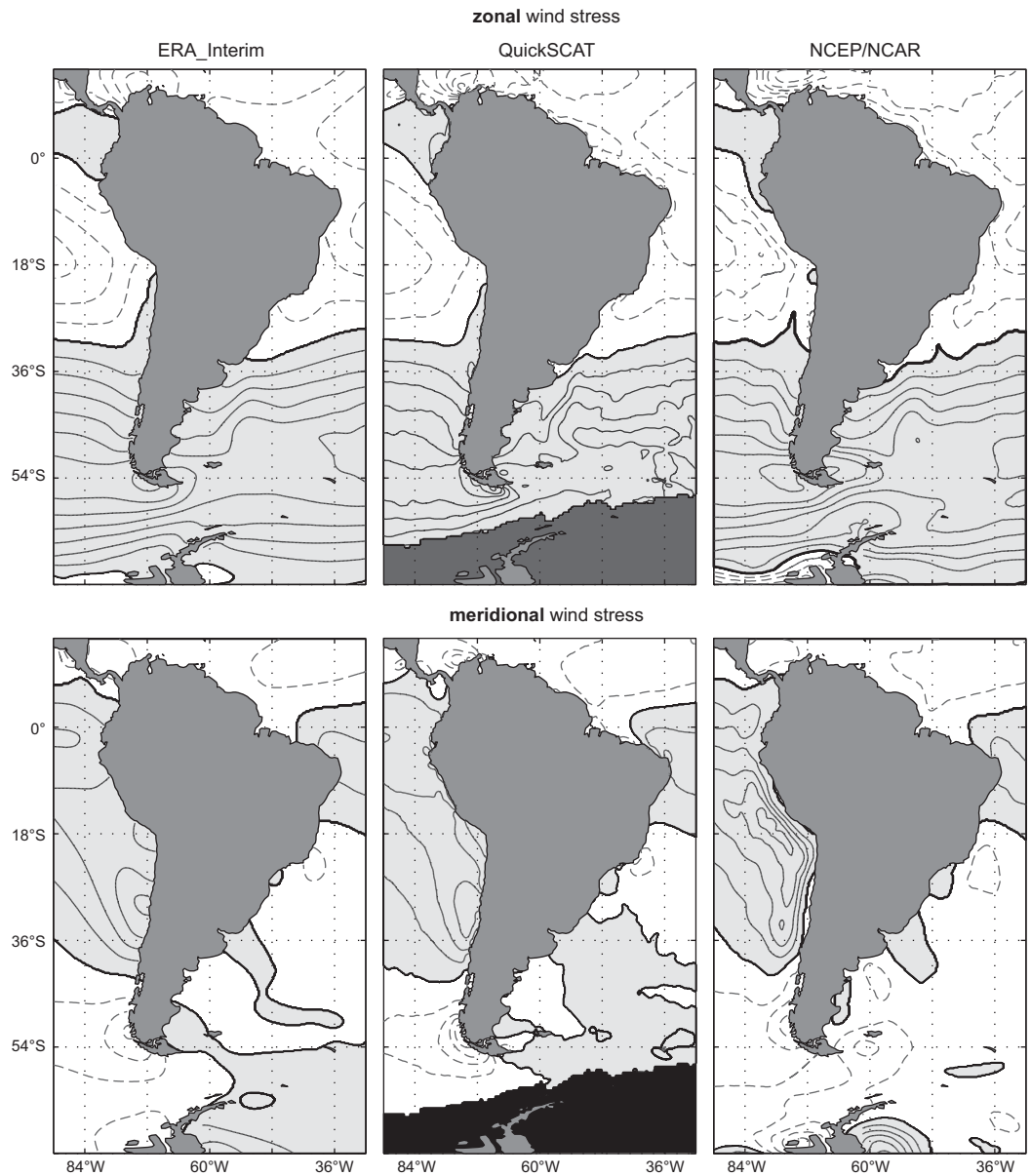
**Figure 2.** (first row) Zonal and (second row) Meridional surface wind stress averaged over the period 2000–2008 derived from the (first column) ERA_Interim, (second column) QuickSCAT, and (third column) NCEP/NCAR data sets. Light gray (white) region corresponds to positive (negative) values. Interval contours are 0.025 N/m$^2$. Dark gray region indicates the sea-ice cover in the QuickSCAT data set.

$$dQdSST = (1) \text{ Infrared contribution} + (2) \text{ Sensible Heat contribution} + (3) \text{ Latent Heat contribution}$$

$$= -4 \cdot \sigma \cdot SST^3 \tag{1}$$

$$= +\rho_{atm} \cdot C_p \cdot C_n \cdot U \tag{2}$$

$$= +\rho_{atm} \cdot C_e \cdot (2.5008 \cdot 10^6 - 2.3 \cdot 10^6 \cdot SAT) \cdot U \cdot 2353 \cdot \ln(10) \cdot q_{sea}/SST^2 \tag{3}$$

where $\sigma = 5.6697 \ 10^{-8}$ W m$^{-2}$ K$^{-4}$ (Stefan-Boltzmann constant), $C_p = 1004.8$ J kg$^{-1}$ K$^{-1}$ (specific heat of atmosphere), $C_h = 0.66 \ 10^{-3}$ (sensible heat transfer coefficient), and $C_e = 1.15 \ 10^{-3}$ (latent heat transfer coefficient). $\rho = 1025$ kg m$^3$ is the water density and $C_p = 3985$ J kg$^{-1}$ C$^{-1}$ is the specific heat for seawater. The monthly mean climatology sea surface temperature (SST), surface air temperature (SAT), wind speed at 10 m (U), atmospheric density ($\rho_{atm}$), and sea level specific humidity (q$_{air}$) are provided by the COADS data

**a-** Amplitude of the tide generating potential (POT$_{amp}$)



**b-** Phase of the tide generating potential (POT$_{phase}$)
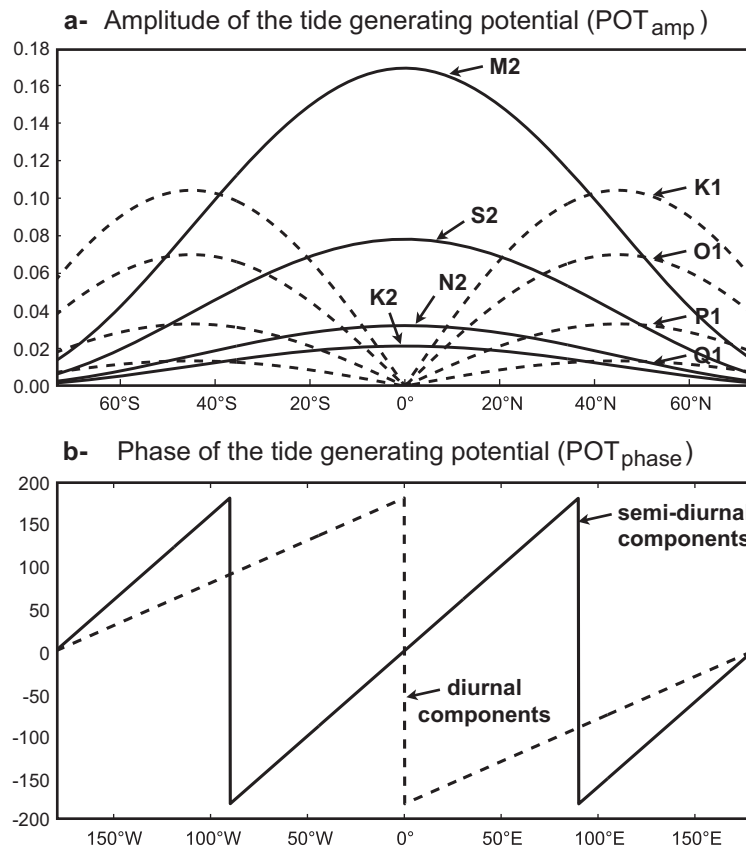


**Figure 3.** (a) Amplitude (in meter) and (b) phase (in degree) of the tide-generating potential for eight tidal constituents (M2, S2, N2, K2, K1, O1, P1, and Q1).

set [*Penven et al.*, 2008]. To account for the lack of an ice module in the ROMS code, the surface water flux is corrected toward the COADS sea surface salinity using the same procedure south of 60°S.

### 2.6. Tidal Forcing

Tides play an important role on the southwestern Atlantic shelf circulation and influence the magnitude of the vertical mixing, in particular over the southern portion of the Patagonian shelf [*Palma et al.*, 2004]. The M2 tide propagates northward along the Patagonian shelf with the largest amplitude (∼3.5 m) and largest current (1.5 m s$^{-1}$) found at the Grande Bay (∼50°S). Tidal forcing is simulated by adding the tide-generating potential to the surface pressure gradient term at each grid cell:

$$P_{surface} = P_{surface} - g * \sum_{itide=M2,S2,...} POT_{amp}(itide) * \cos\left(\frac{2\pi}{T(itide)}t + POT_{phase}(itide)\right)$$

where $P_{surface}$ is the model pressure at the surface, $g = 9.81$ m s$^{-2}$, and itide the tidal period (e.g., 12.42 h for the M2 component). The amplitude and phase of the tide-generating potential ($POT_{amp}$, $POT_{phase}$) of the first eight tidal components (semidiurnal: M2, S2, N2, K2; diurnal: K1, O1, P1, Q1) are illustrated on Figure 3. Throughout this section, only the highest amplitude signal over the Patagonian shelf M2 has been simulated.

To define the tidal forcing at the northern (open) boundary of the model and for the sake of consistency, we run a global version of our model with a horizontal resolution of ¼° and forced with the M2 tidal potential only. The amplitude and phase of the M2 harmonic produced by this simulation are in good agreement with the values inferred from the TOPEX/POSEIDON global tidal model (TPXO; Figure 4a). We impose this solution at the northern boundary of the nested model and run this model forced with the tide-generating
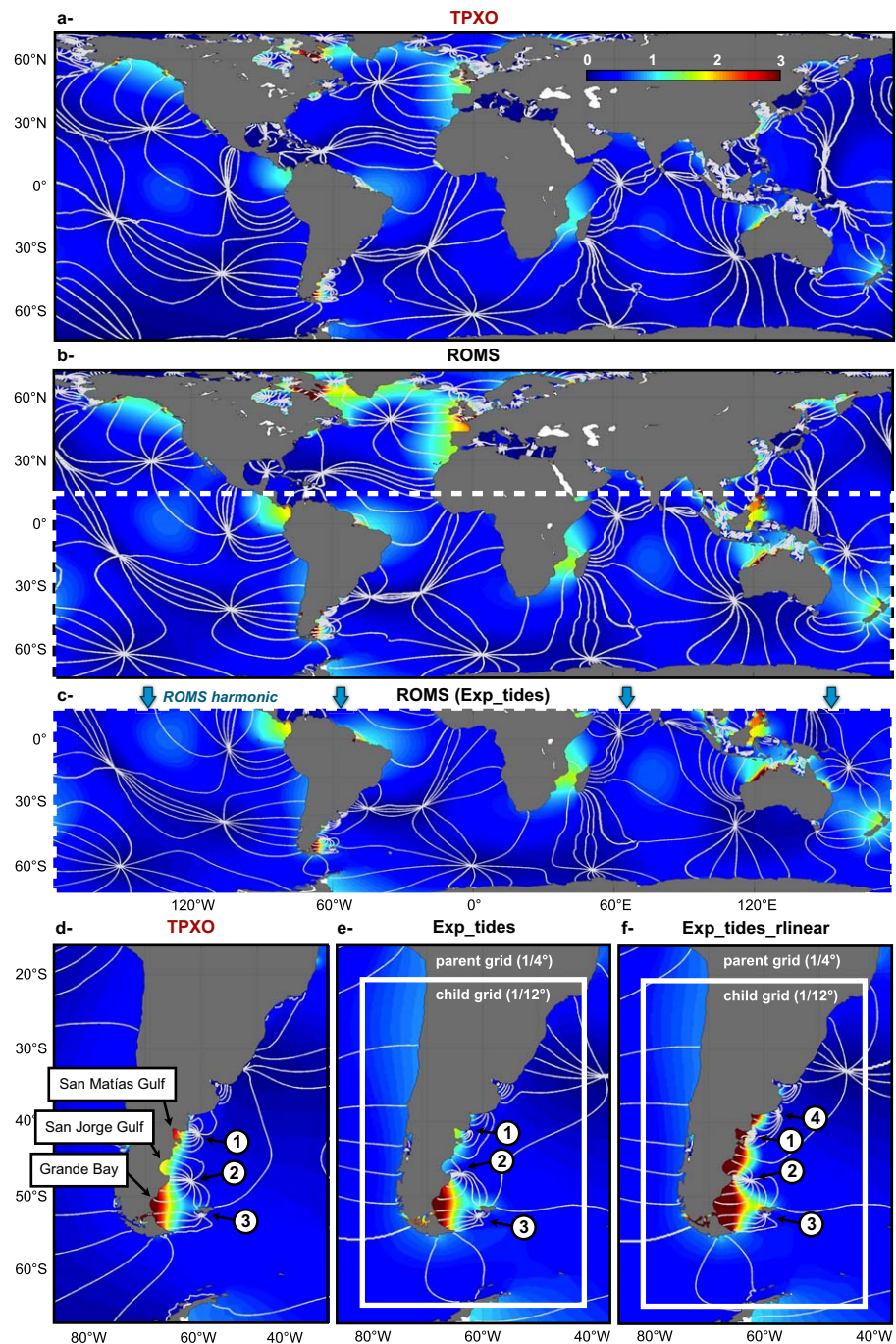
**Figure 4.** Amplitude (in meters) and phase (white contours; 30° contour intervals) of the M2 tidal constituent produced by the (a) TPXO.7 and (b and c) ROMS models. Figure 4b is the solution using a global grid (no open boundary). (c) Solution of the South American grid forced by the solution (Figure 4b) at the northern boundary (∼15°N). (e and f) Solutions of the two-ways nesting experiments Exp_tides (quadratic bottom stress) and Exp_tides_rlinear (linear bottom stress). 1, 2, 3, 4 highlight four amphidromic points.

potential. There is also good agreement between the tides produced by the nested model, TPXO [*Egbert and Erofeeva*, 2002], and the study of *Glorioso and Flather* [1995] (Figure 4d). Over the Patagonian shelf, both the ROMS and TPXO M2 tidal harmonics exhibit three amphidromic points (labeled "1," "2," and "3"). Although the ROMS amphidromic points are located more onshore than in the TPXO solution, the phase and amplitude of the M2 tidal component over the southern Patagonian shelf seem to be well reproduced (∼3.5 m amplitude at Grande Bay). Experiments using different quadratic bottom stress ranging from $\alpha_{quad} = 0.003$ to 0.007 (equation of the bottom stress parameterization on section 2.9) show very little

changes in the phase and slightly higher amplitude over the Grande Bay, San Jorge Gulf, and San Matias Gulf more likely to the TPXO solution (not shown). Differences are however significant when using a linear parameterization of the bottom drag (Exp_tides_rlinear; $\alpha_{linear}$ = 0.0003 m s$^{-1}$). Figure 4f shows indeed an overall overestimate along the Patagonian shelf with amplitude up to 7 m at Grande Bay and a forth amphidromic point.

### 2.7. Lateral Boundary and Initial Conditions

The parent model has only one open boundary located at 15°N. There, we impose a modified radiation boundary condition [*Marchesiello et al.*, 2001] with nudging to the monthly mean climatology provided by the high-resolution Modular Ocean Model (MOM3)-based Ocean General Circulation Model code optimized for the Earth Simulator (OFES; global 0.1° ocean circulation model) [*Masumoto et al.*, 2004; *Sasaki et al.*, 2004, 2008]. The initial condition is obtained from the OFES global ocean model for the month of January.

### 2.8. Mixing Parameterization

The model equations are based on an upstream third-order advection scheme, in which the diffusion of tracers (temperature and salinity) is split from the advection term and where diffusion is represented by a biharmonic diffusivity satisfying the Peclet constraint [*Marchesiello et al.*, 2009]. For the control run (section 3), horizontal mixing of momentum is preferred to mixing along $\sigma$-coordinates. For vertical mixing, our configuration uses a K-Profile Parameterization (KPP) scheme in the surface boundary [*Large et al.*, 1994]. No explicit diffusion and viscosity have been added to the high-order diffusive schemes of the model.

### 2.9. Bottom Friction Parameterization

ROMS includes the following linear and a quadratic bottom stresses formulation:

$$(\tau_{bx}, \tau_{by}) = \left( u_b \left[ \alpha_{lin} + \alpha_{quad}(u_b^2 + v_b^2)^{1/2} \right], v_b \left[ \alpha_{lin} + \alpha_{quad}(u_b^2 + v_b^2)^{1/2} \right] \right)$$

where $(\tau_{bx}, \tau_{by})$ is the bottom stress in the zonal and meridional directions and $(u_b, v_b)$ are the zonal and meridional components of the bottom velocity. A biharmonic parameterization of the bottom stress with a constant value of $\alpha_{quad}$ = 0.007 is applied to the control run (Exp_CTRL; section 3).

## 3. The Mean Circulation

Exp_CTRL was started from rest and it was forced with the ERA-Interim wind stress data (Table 1). The parent model was integrated in a stand-alone mode for 10 years after which the nested (child and parent) model was integrated for another 15 years, the last 10 years are used in the present analysis.

The large-scale circulation patterns produced by the nested model are in good agreement with observations (Figure 5). The circulation in the subpolar region (south of ~45°S) is dominated by the eastward flow of the ACC, which, in our simulation, has a mean volume transport of 132 Sv (Figure 5b). This value is in good agreement with the observational estimates of 134 ± 12 Sv by *Whitworth and Peterson* [1985] and 136.7 ± 7.8 Sv by *Cunningham et al.* [2003]. A cross section of the model velocities at the Drake Passage shows that the ACC is composed of three major jets that correspond with the Sub-Antarctic Front (SAF), the Polar Front (PF), and the southern ACC front (sACCf) [*Nowlin and Klinck*, 1986; *Orsi et al.*, 1995] (Figure 9a). The westward flow of the Antarctic Coastal Current dominates the circulation along the coast of Antarctica. This current is driven by the wind stress and by buoyancy forcing [*Tchernia and Jeannin*, 1980; *Tchernia*, 1981; *Núñez-Riboni and Fahrbach*, 2009].

The MC is formed by the northernmost jet of the ACC, which, after leaving the Drake Passage, flows northward along the continental slope of Argentina until approximately 38°S where it collides with the poleward flow of the BC. Estimates of the MC mean transport range between 41 and 45 Sv at 41°S [*Vivier and Provost*, 1999; *Maamaatuaiahutapu et al.*, 1998; *Palma et al.*, 2008]. These values are in agreement with Exp_CTRL, which produces a volume transport of 40 Sv at 41°S (Figure 5b; thick turquoise line). Although the MC originates from the ACC the transport variations of the two currents are poorly correlated due to the transit of high-frequency waves originating in northern portion of the Drake Passage [*Fetter and Matano*, 2008].

The BC forms near 15°S feeding from the westward flow of the South Equatorial Current. In our simulation, the BC transport increases from 4 Sv at its origin to a maximum of ~40 Sv at 33°S (Figure 5c). This value is
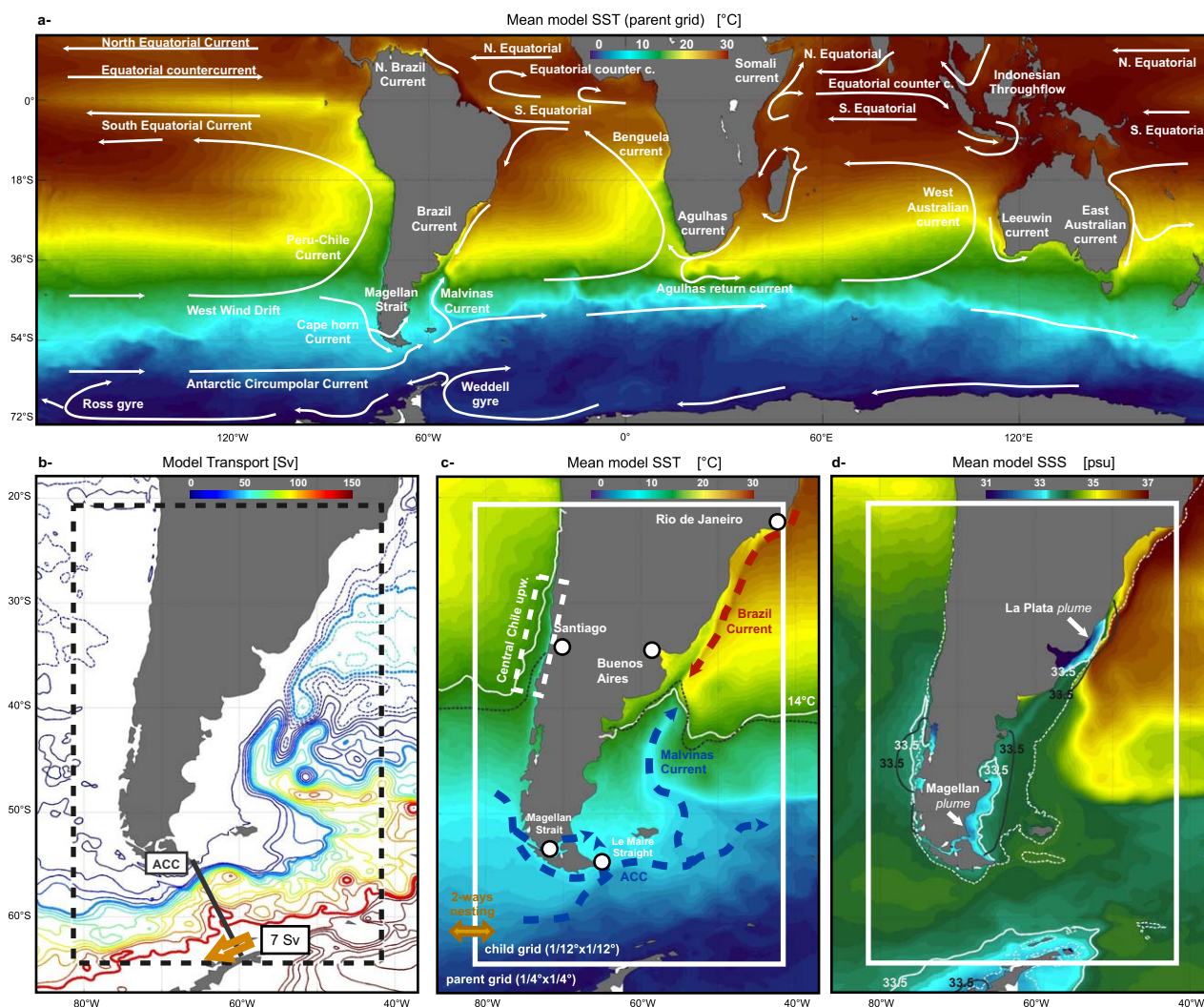
**Figure 5.** (a–c) Mean model Sea Surface Temperature (SST). The model parent grid encompasses the entire southern hemisphere from Antarctica to 15.2°N (1/4° × 1/4° resolution), the nested grid covers the region defined by the white rectangle (1/12° × 1/12° resolution). Figure 5b shows the vertically integrated transports (contour interval of 10 Sv). The thick turquoise contours correspond to the 40 and 130 Sv Transports. (d) Mean model sea surface salinity (SSS). The white and dashed grey contours on Figure 5c (Figure5d) correspond to the 14°C isotherm (33.5 psu isohaline) of the mean model SST (SSS) and mean satellite Pathfinder SST (World Ocean Atlas salinity), respectively. Dashed white line of Figure 5d corresponds to the 200 m isobath.

larger than the early estimates of 18 Sv by *Peterson and Stramma* [1991], who assumed a level of no motion at 1500 m and, therefore, did not include the poleward volume flux of the deep western boundary current [*Meinen et al.*, 2012]. This deep current can be observed in a vertical, cross-shelf section at 33°S (Figure 6a). A similar poleward flow is also observed in the HYbrid Coordinate Ocean Model simulation (Figure 6b). Note that, by considering the BC as the flow only above 1000 m (i.e., omitting the contribution of the deep western boundary current), the total transport decreases from 40 to 27 Sv at 33°S. After separating from the coast, the BC splits into two branches, one retroflecting to the north, where it generates a recirculation cell and the other flowing farther south as shown by observations [e.g., *Saraceno et al.*, 2004]. The retroflection of the BC is accompanied by the continuous generation of warm core rings, which are also consistent with observations [*Olson et al.*, 1988].

The collision of the MC and the BC near 38°S generates a region of intense mesoscale variability that is also influenced by the injection of freshwaters from the La Plata River (Figure 5d) [*Piola et al.*, 2008]. The location of the BMC is determined by the momentum balance between the MC and the BC and it is, therefore, highly sensitive to the particular representation of the bottom topography and the spatial distribution of the volume transport of the ACC at the Drake Passage [*Matano*, 1993; *Agra and Nof*, 1993]. Numerical simulations
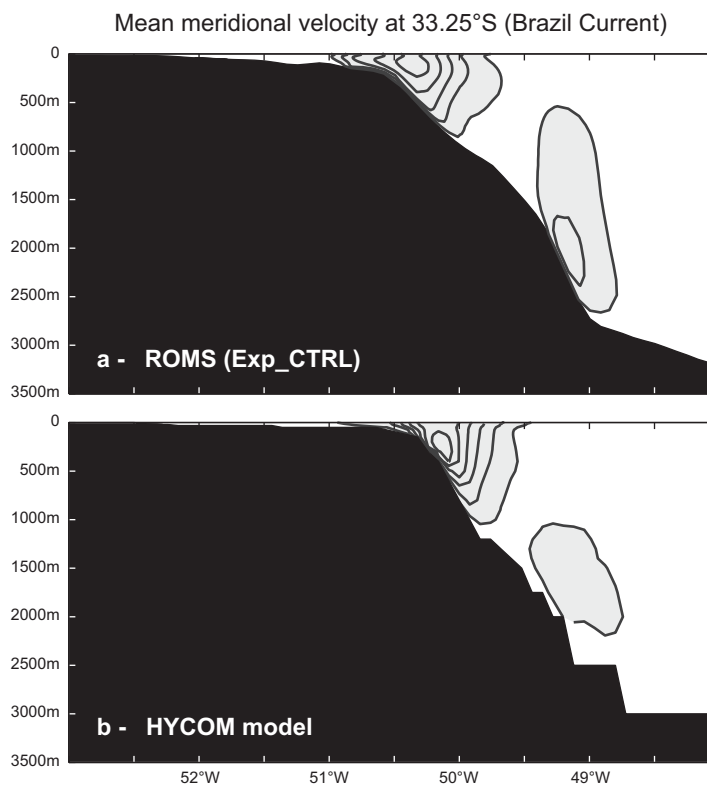
**Figure 6.** Mean Meridional velocity [m/s] at 33.25°S across the Brazil Current for (a) Exp_CTRL and (b) over the year 2012 of the Data-Assimilation HYCOM model. Contour interval is 0.1 m/s. Light gray region indicates velocity greater than 0.1 m/s.

have also shown that the location of the BMC is very a sensitive to the horizontal and vertical resolution of the models as well as to the particulars of the momentum advection scheme and bottom friction parameterization [*De Miranda et al.*, 1999; *Treguier et al.*, 2001; *Barnier et al.*, 2006]. The location of the BMC and the regional patterns of eddy kinetic energy in Exp_CTRL are in agreement with observations (Figures 5 and 7). Model and observations show high values of eddy kinetic energy (EKE) along the ACC path and at the BMC, where the eddy activity featuring the characteristic C-shape that extends from the BMC toward the southern limit of the Argentine basin (Figure 7).

Although Exp_CTRL is able to represent reasonably well the overall structure of the western boundary system in the southwestern Atlantic region it is unable to simulate the Zapiola Anticyclone, an anticlockwise vortex that is centered at approximately 44°S 45°W with an overall transport of approximately 100 Sv [*Saunders and Kings*, 1995]. Sedimentological records indicate that this vortex has been a feature of the regional circulation for thousands of years [*Flood and Shor*, 1998]. *Dewar* [1998] posited that the Zapiola Anticyclone is forced by potential vorticity fluxes generated by the eddy field and that its intensity it is controlled by bottom friction. The only numerical model that has been able to reproduce this vortex is the one described in *De Miranda et al.* [1999]. As we shall show the Zapiola Anticyclone is correctly reproduced if the magnitude of the bottom stress is reduced, a result that is in agreement with previous findings [*De Miranda et al.*, 1999].

## 4. Sensitivity Experiments

In this section, we discuss the sensitivity of the southwestern Atlantic circulation to the atmospheric forcing and the model parameterizations.

### 4.1. Sensitivity to the Wind Stress Forcing

To test the sensitivity of the model to the use of different wind stress climatologies, we run the experiment Exp_NCEP, which was forced with the NCEP/NCAR climatology and the experiment Exp_QSCAT, which was
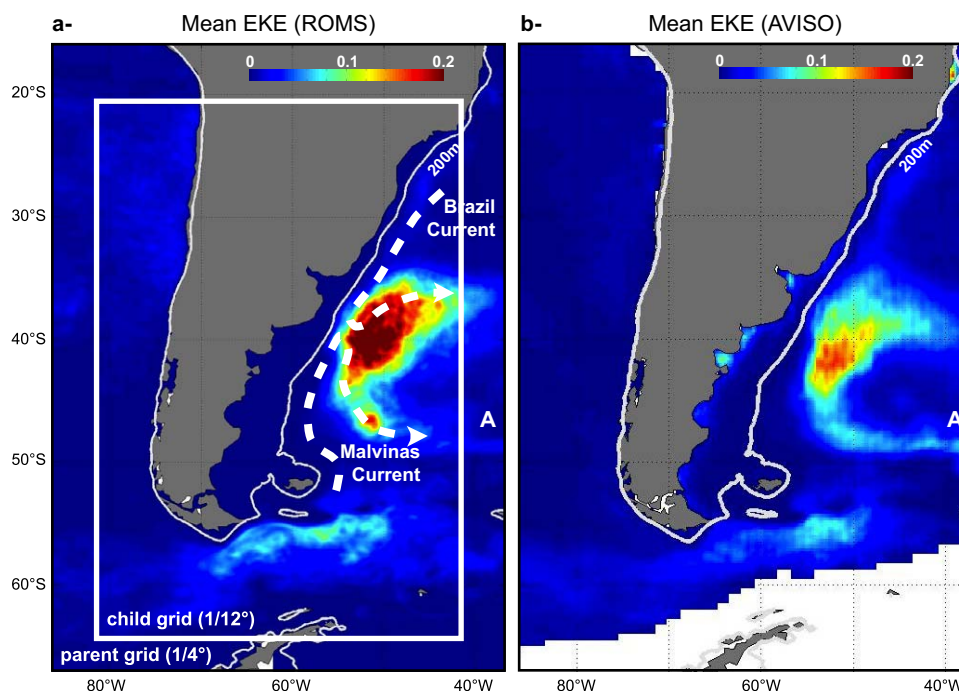
**Figure 7.** Mean Eddy Kinetic Energy [$m^2 s^{-2}$] derived from the geostrophic current from the (a) ROMS simulation and (b) AVISO satellite data.

forced with the QuickSCAT climatology. In Exp_NCEP, the ACC transport decreases from 130 to ∼113 Sv, while in Exp_QSCAT the ACC transport remains unchanged (Figure 8). The observed decreased in the Exp_NCEP is associated with a strengthening of the Antarctic Coastal Current (Figure 9), which decreases the averaged transport through the Drake Passage (Figures 8a–8d). The change, however, is confined to the proximities of the Antarctic continent. Thus, north of 61°S the three wind stress data sets produce a comparable structure of the ACC (Figure 9). As expected, and since the MC depends on the ACC transport on the northern portion of the Drake Passage [*Matano*, 1993], the three experiments produce similar MC transports and hence are able to correctly position the location of the BMC (Figures 8b and 8c). The BC transport is also very similar among the three experiments (dashed stream functions on Figures 8b and 8c), which is expected since the BC is largely driven by the wind stress curl over the South Atlantic [*Matano et al.*, 1993] and the main differences between the three wind stress climatologies are observed near coastal regions.

It has been shown that small-scale SST feedbacks generate anomalies in the wind stress curl in regions of large temperature gradients such as the Patagonia's shelf break front and the BMC region (Figure 2) [*Tokinaga et al.*, 2005; *O'Neill et al.*, 2012]. *Saraceno et al.* [2005] posited that local northerly winds seem associated with springs and summer chlorophyll maxima observed on the onshore side of the MC [*Romero et al.*, 2006; *Garcia et al.*, 2008; *Painter et al.*, 2010]. To test this hypothesis, we run an additional experiment that is similar to Exp_CTRL but forced with the wind stresses derived from the QuickSCAT data, which includes the wind stress curl anomalies driven by the SST gradients (Figure 10). These anomalies are not present in the ERA_Interim wind stress data used in Exp_CTRL. A comparison of vertical velocities between both experiments shows that the magnitude of the shelf break upwelling remains largely unchanged in the two experiments (Figure 10). Thus, the experiment driven with the QuickSCAT wind stress produces a similar upwelling regime than the experiment driven with the ERA_Interim wind stress. This result is consistent with the shelf break upwelling theory posited by *Matano and Palma* [2008], who argued that the shelf break upwelling of Patagonia is driven by interaction of the MC and the bottom topography. According to this theory the magnitude of the Patagonian shelf break upwelling is proportional to the transport of the MC, which, in turn, is proportional to the winds integrated over the entire Southern Ocean and it is therefore largely unaffected by local wind stress forcing
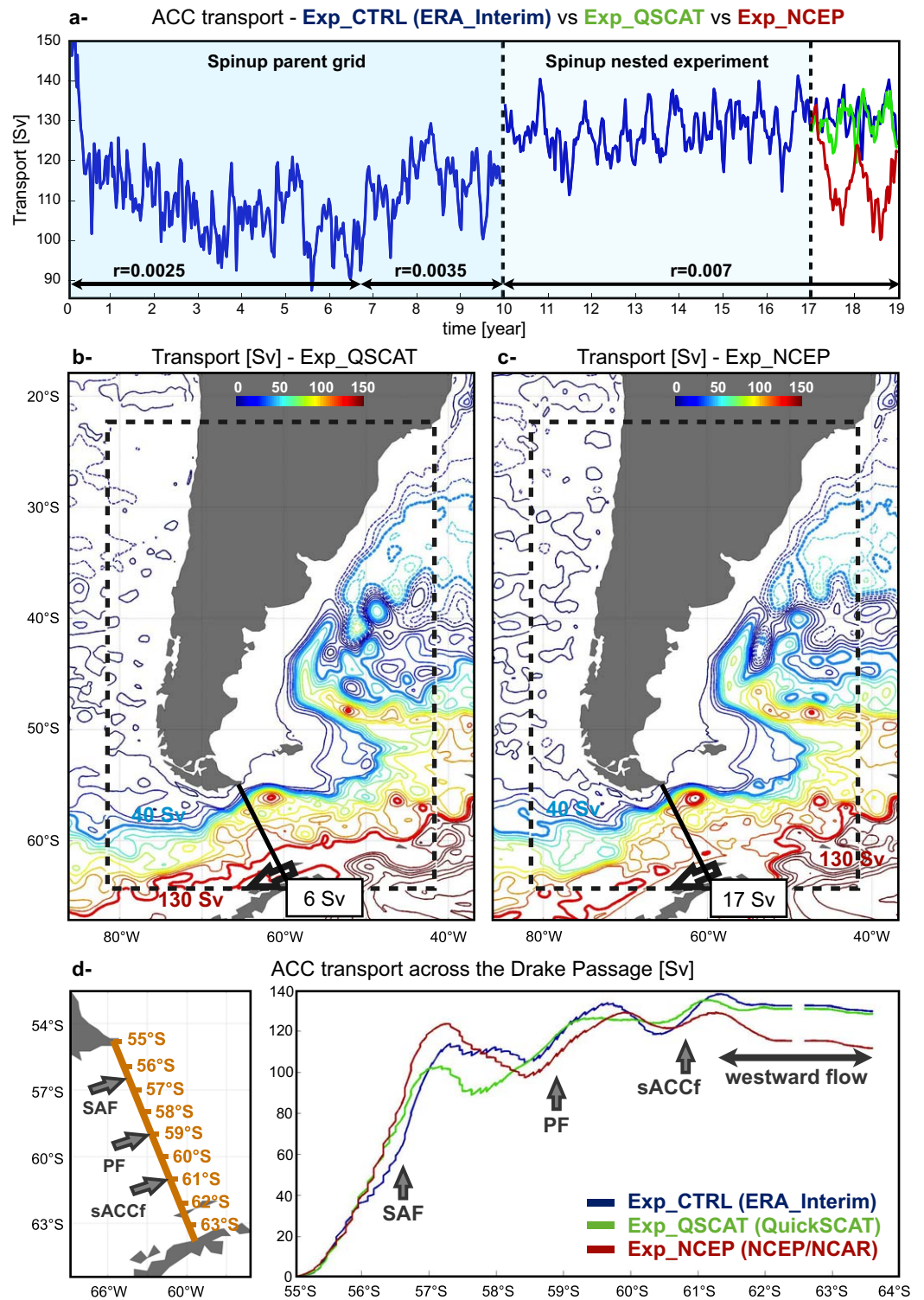
**Figure 8.** (a) The Antarctic Circumpolar Current (ACC) across the Drake Passage from the initial condition. During the spinup of the parent grid, the bottom stress parameter (r) has been changed and referred in Figure 8a. b and c correspond to the vertically integrated transport (contour interval of 10Sv) and the thick contours to the 40 and 130 Sv transports, respectively, for Exp_QSCAT and Exp_NCEP (same as Figure 4b). (d) The Latitudinal variation of the ACC transport across the Drake Passage from Exp_CTRL (blue line), Exp_QSCAT (green line), and Exp_NCEP (red line).
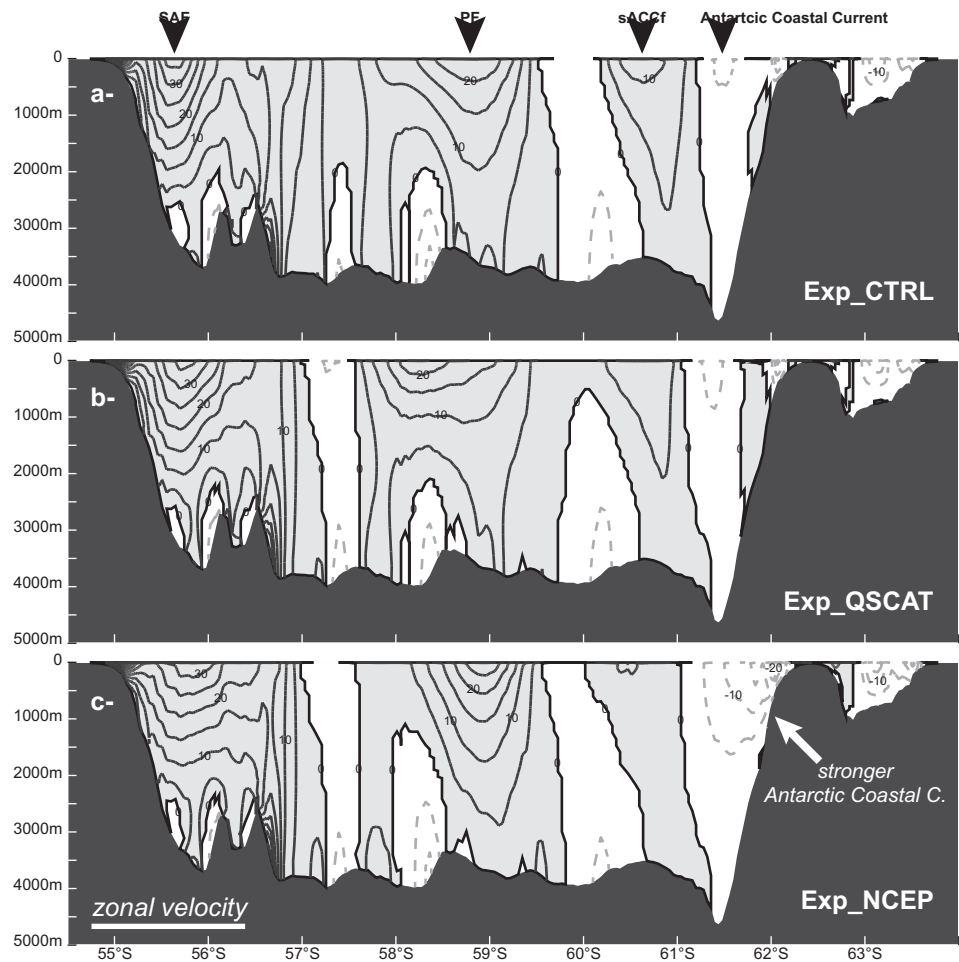
**Figure 9.** Model Zonal velocity across the Drake Passage [cm/s]. Contour interval is 5 cm/s. Light gray region indicates positive values. SAF, SF, and sACCf stand for "Sub-Antarctic Front," "Polar Front," and "southern ACC front," respectively.
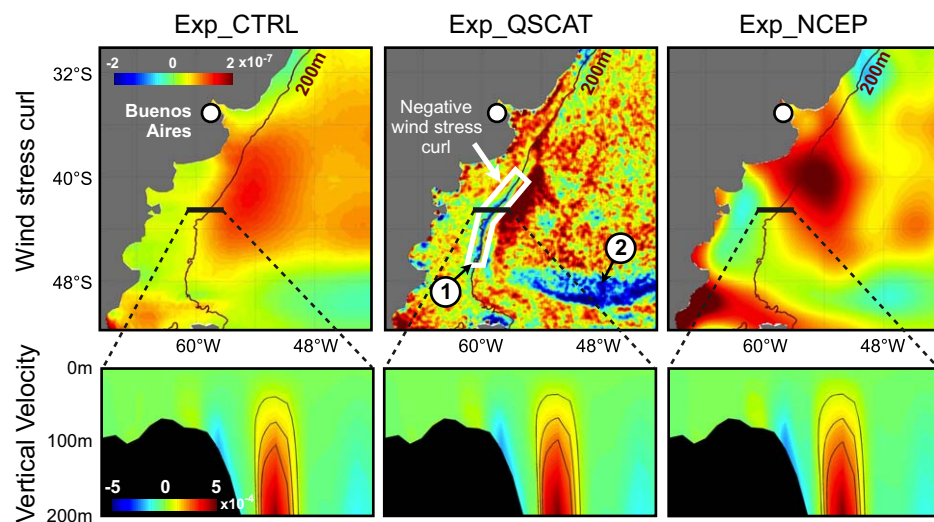


**Figure 10.** Surface wind stress curl [Pa m$^{-1}$] and Vertical velocity [m s$^{-1}$] across the black line. Black contours correspond to 1, 2, and 3.10 m s$^{-1}$.

### 4.2. Sensitivity to the Bottom Friction Parameterization

As mentioned above, previous studies have shown that the southwestern Atlantic circulation is sensitive to the parameterization of bottom friction, which impacts on the model's ability to correctly represent the location of the BMC and to develop the Zapiola Anticyclone [*Barnier et al.*, 2006; *De Miranda et al.*, 1999; *Penduff et al.*, 2001]. This sensitivity is expected since the flow in the subpolar region is predominantly barotropic and hence highly susceptible to the influence of the bottom topography. To test the sensitivity of our model to the parameterization of bottom friction, we ran an additional experiment (Exp_r3) which uses a smaller bottom stress parameter $\alpha_{quad} = 0.003$ than Exp_CTRL ($\alpha_{quad} = 0.007$).

In agreement with previous studies, Exp_r3 shows a significant influence of the bottom stress parameterization on the location of the BMC (Figure 11a). The BMC is located at $\sim39.0°$ in Exp_CTRL but it moves to $\sim37.0°$S, in Exp_r3. This northward shift is associated with an increase of the MC transport that is driven by an intensification of the northernmost jet of the ACC at the Drake Passage, which increases its transport in $\sim20$ Sv north of 57°S (Figure 11e). Half of this increment is funneled into the MC and toward the BMC (Figures 11c and 11d). At 42°S, 41°S, and 40°S the MC transports, respectively, 65 (72), 40 (47), and 17 Sv (40 Sv) in Exp_CTRL (Exp_r3). The BC transport is less affected by changes in the bottom stress due to its high baroclinic structure [*Da Silveira et al.*, 2004].

One of the most striking consequences of diminishing the bottom friction is the development of the Zapiola Anticyclone, which is a 10° wide vortex centered at 44°S 45°W and having a transport of 105 Sv (Figure 11d). To further test the sensitivity of the Zapiola Anticyclone to the bottom friction parameterization, we performed an additional experiment increasing the bottom friction parameter to $\alpha_{quad} = 0.0045$. In this experiment, the magnitude of the Zapiola Anticyclone is reduced to 90 Sv. This result is consistent with the conclusions of *De Miranda et al.* [1999], whom noted a nearly linear correlation between bottom drag and strength of the Zapiola Anticyclone. As expected, the development of the Zapiola Anticyclone improves the realism of the regional circulation, leading to a more realistic EKE distribution of this region (higher EKE along the southern boundary of the Zapiola Anticyclone; not shown).

## 5. The Seasonal Variability of the Southwestern Atlantic Circulation

The seasonal variability of the southwestern Atlantic circulation is evaluated with the experiment Exp_SEASON, which is an updated version of Exp_CTRL in which we set $\alpha_{quad} = 0.0045$ to correctly simulate the development of the Zapiola Anticyclone and the position of the BMC (Figure 12). In Exp_SEASON, the ACC transport at the Drake Passage has a relatively minor seasonal variation with a maximum of $\sim135$ Sv during the austral spring (September-October-November) and a minimum of $\sim130$ Sv during the austral winter (June-July-August; Figure 13). The weak seasonality of the ACC transport in Exp_SEASON is consistent with the previous findings of *Fetter and Matano* [2008], who reported that the seasonal variations of the ACC transport are less than 2% of its total transport. The amplitude and phase of the seasonal variations of the ACC transport in the Drake Passage vary in the meridional direction. North of 56°S, the transport peaks during March-April (Figure 13). Using particle tracking, we determined that a change of transport at the Drake Passage takes 3–4 months to reach the MC cross section at $\sim41°$S. Thus, the MC transport reaches a maximum of 78 Sv during the austral winter and a minimum of 68 Sv during the austral summer (Figure 13). The seasonal changes of the MC transport in Exp_SEASON are consistent with those inferred from satellite sea surface height data, which shows similar seasonal differences in the geostrophic velocities between the austral winter and the austral summer (Figure 14c). Our simulation indicates that the seasonal variations of the MC transport are largely concentrated in the offshore portion of the current, while the inshore portion—which encompasses the portion of the current that defines the location of the BMC—shows no significant seasonal variations (Figure 14b). Note that, although we based our separation of the inshore and offshore MC on seasonality, it also coincides with the presence of two permanent jets (Figures 14a and 14b; see section 7). This feature of our numerical simulation is consistent with satellite sea surface height data, which shows that the stronger seasonal differences in the geostrophic velocities are between the austral winter and the austral summer (Figure 14c). *Spadone and Provost* [2009] observed that the seasonal variability of the MC transport however shows significant interannual variations. Using data encompassing the period 1992–2007, they report that for the 1992–1997 period the intraannual variability of the MC transport was concentrated on relatively short periods (50–90 days, while during the period 2000–2006 the seasonal
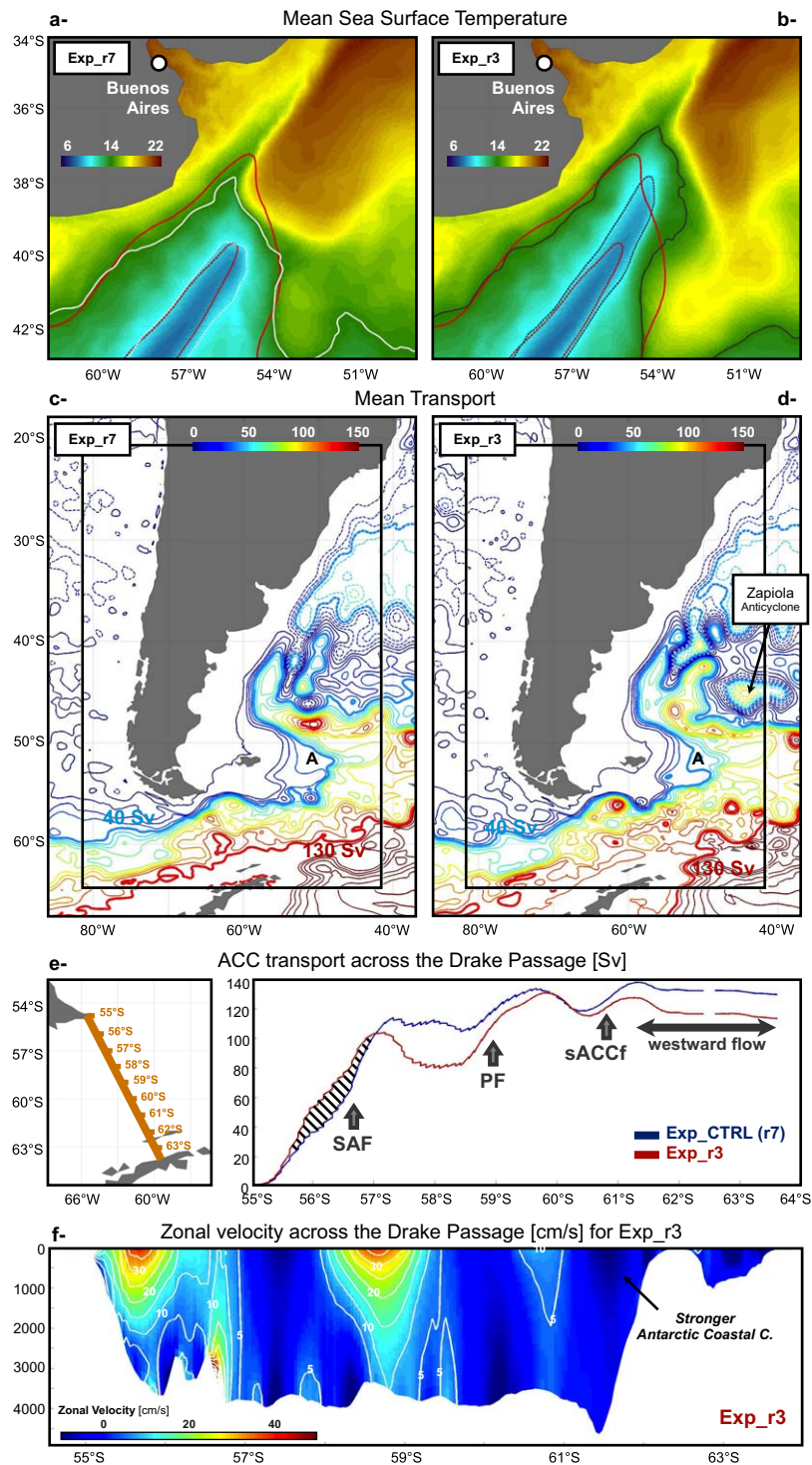
**Figure 11.** (a andb) Mean Sea Surface Temperature from Exp_r7 (i.e., Exp_CTRL) and Exp_r3. The dotted and solid contours correspond to the 10°C and 14°C isotherms. Red, white, and black contours correspond, respectively, to the Satellite, Exp_r7, and Exp_r3. (c and d) Same as Figure 5b. Dashed contours correspond to negative transports. (e) Same as Figure 6d. (f) Same as Figure 7. Differences between Figures 11c and 5b result from the fact that Figure 11c shows a 1 year average while Figure 5b shows a 7 years average.

variations become more dominant with stronger MC during austral winter). The MC transport in our simulation also shows interannual variations but since the model was forced with climatological winds those variations are caused by internal ocean dynamics and cannot be directly compared with observations.
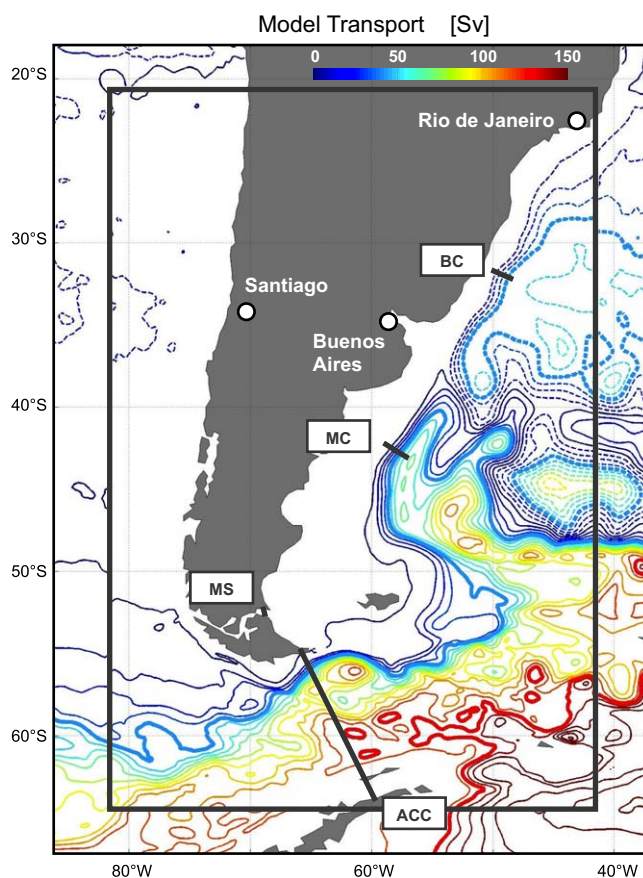
**Figure 12.** Mean vertically integrated transports (contour interval of 10 Sv).

The seasonal variations of the BC transport in Exp_SEASON oppose those of the MC, it increases during the austral summer and weakens during the austral winter (Figure 13). Note that the contribution of the deep water boundary current (Figure 6) does not impact significantly the seasonal variability of the BC transport (not shown). Previous studies have shown that these changes are related to the variations of the wind stress curl over the southern portion of the subtropical gyre [*Matano et al.*, 1993; *Wainer et al.*, 2000]. The seasonal cycle of the zonally averaged wind stress curl exhibits a significant latitudinal dependence (Figure 15b). Over the subtropical gyre the variations of the wind stress forcing, which intensifies during the austral winter and weakens toward the summer, are in opposite phase to the variations of the BC transport. The seasonality of the wind stress curl reverses south of 35°S intensifying during the summer and weakening toward the winter. To highlight the spatial structure of the seasonal variations of the wind stress curl, we calculated the Empirical Orthogonal Functions of the wind stress curl anomalies. The first EOF, which explains 71% of the total variance (Figures 15c and 15d), corresponds to an intensification of the wind stress curl over the subpolar region during the austral summer. This intensification leads to the observed increases of the BC transport during that season. There is good agreement between the first EOF and the seasonal variations of the BC transport (Figure 13).

The second EOF of the wind stress curl explains 16.4% of the total variance and it has a stronger coastal signature, with maximum amplitudes over the Cabo Frio upwelling region (Figures 15e and 15f). The temporal variations of this mode are consistent with the upwelling events described by *Castelao and Barth* [2006] (Figure 15f). Further analysis of the model results show a high correlation between the upwelling index calculated from the wind stress and the upwelling velocities calculated from our model (Figure 15f). The differences between the upwelling index and the time series of the second EOF are partly associated with the fact that a portion of the upwelling variability is also projected into the first EOF (Figures 15b and 15c).

Previous studies have posited that the seasonal changes of the MC and the BC transport generate meridional displacements of the BMC [*Olson et al.*, 1988; *Matano et al.*, 1993]. To quantify these displacements, we define the latitude of the BMC in Exp_SEASON as the location where the 1000 m isobath intersects the 10°C isotherm at 200 m (Figure 16a). This definition, which follows *Goni and Wainer* [2001], is in good agreement with the proxy used by *Goni et al.* [2011] as the maximum SST gradient along the 1000 m isobath (Figure 16a). The location of the BMC in Exp_SEASON varies from 36°S to 40°S, and it has a clear tendency for being located more to the south during the austral summer and to transition toward the north during the fall and winter (Figure 16a). To further evaluate the kinematics of the BMC we computed the mean stream fuction for the austral summer and the austral winter (Figure 16b). The stream function shows a seasonal alongshelf migration of the BC, which is consistent with its seasonality (Figure 13), but no significant seasonal
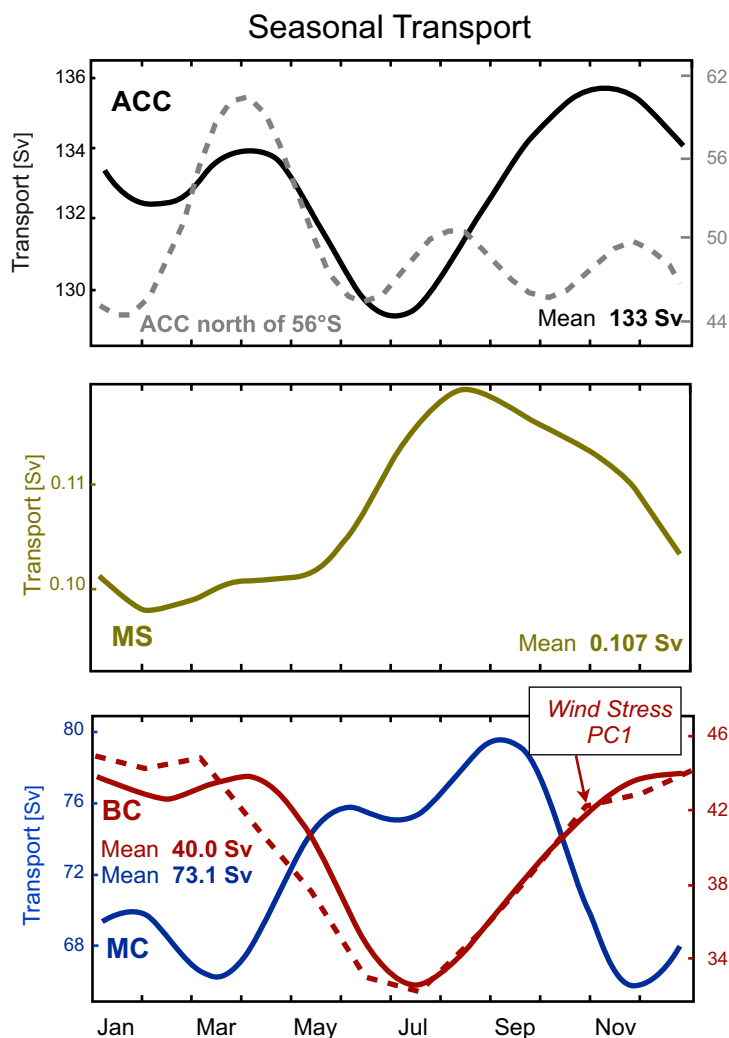
**Figure 13.** Seasonal cycle of the Antarctic Circumpolar Current (ACC; black line; the Antarctic Coastal Current has been removed), Brazil Current (BC; red line), Malvinas Current (MC; blue line), and Magellan Strait outflow (MS; green line). The gray dashed line corresponds to the seasonal variability of the northern portion of the ACC. The red dashed line is the Principal Component (PC) of the wind stress curl (Figure 8d).

displacements of the MC. Over the shelf, the more eastward penetration of the streamlines during the austral winter (black line on Figure 16b) responds to a stronger eastward wind stress field over the shelf during winter (vectors on Figure 16b).

## 6. The Shelf Break Upwelling of Patagonia

One of the most distinct characteristics of the southwestern Atlantic shelf region is the narrow and persistent chlorophyll-a bloom that develops during the springtime along the shelf break of Patagonia [*Romero et al.*, 2006; *Garcia et al.*, 2008]. *Matano and Palma* [2008] and *Miller et al.* [2011] argued that this bloom is associated with the upwelling of nutrient-rich waters along Patagonia's shelf break. They posited that bottom friction produces a cross-shelf divergence of the MC transport that leads to shelf break upwelling. Matano and Palma hypothesis is corroborated by our model results, which show the development of strong upwelling cells along the Patagonian shelf break. *Matano and Palma*'s [2008] model did not consider the

impact of realistic bathymetry, e.g., canyons, changes of bottom slope, etc., that lead to substantial modifications of the upwelling configuration. To assess the variability of Patagonia's shelf break upwelling and its relation to the MC transport, we constructed an upwelling index, which is defined as the time series of the vertical velocity integrated from 200 m to the surface and averaged over the box region shown in Figure 17a, and compared it with the time series of the MC transport. In agreement with *Matano and Palma*'s [2008] theory, Exp_SEASON shows a high correlation between the time variability of the upwelling index and the MC transport. The variability of the transport of the inshore portion of the MC correlates more strongly to the upwelling variability ($R = 0.66$; Figure 17c) than the variability of the total transport of the MC, ($R = 0.33$). The correlation appears to be robust to the chosen period of analysis, since an ancillary calculation using the 14 years of nested integration shows a similar correlation ($R = 0.61$).
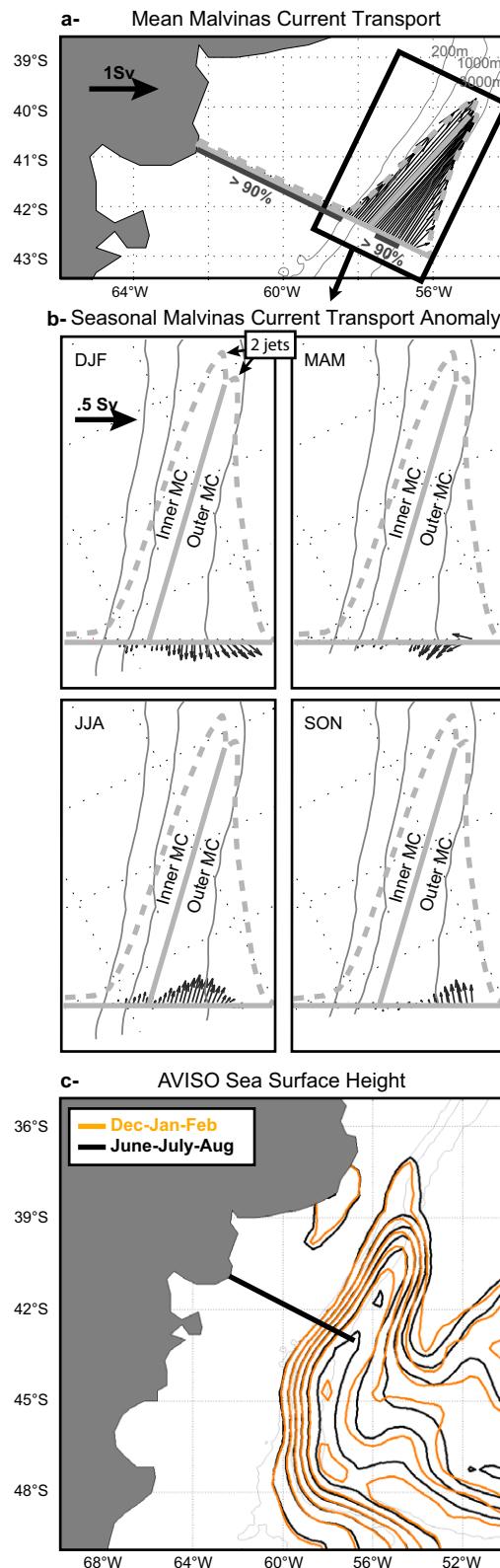
## 7. The Multiple Jets of the MC

Recent studies suggest that the MC transport is not uniformly distributed in the cross-shelf direction flow but it is unevenly distributed in several narrow jets. *Franco et al.* [2008] identified a distinct thermal front at

**Figure 14.** Arrows show the (a) mean and (b) seasonal anomalies of the Malvinas Current transport across the black transect. Percentages delimit the regions where the seasonal variability is significant. (c) Compares the satellite AVISO Sea Surface height for austral summer and winter.

the Patagonian shelf break (∼200 m isobath) and two additional fronts at approximately 40 km in the inshore and offshore directions. The close correspondence between the location of these fronts and the planetary vorticity contours suggested the existence of multiple jets although such jets could not be confirmed with the SST data. In a later study, *Piola et al.* [2013] used in situ and remote observations to argue that the core of the MC is formed by two main jets, flowing along the 200 and 1400 m isobaths, and a series of secondary and discontinuous high-velocity cores. These jets extended from 52°S to 42°S, thus encompassing a meridional extent of approximately 900 km. *Piola et al.* [2013] noted that none of the observations used in their analysis are conclusive but that the overall agreement among different data sources suggests that multiple jets are a robust feature of the MC's velocity structure. Previous numerical studies are, to some extent, consistent with *Piola et al.*'s [2013] conclusions. *Fetter and Matano* [2008], for example, reported that in a global, eddy-permitting numerical simulation the northernmost jet of the ACC splits into two branches after leaving the Drake Passage. These branches flow along the Malvinas Plateau and merge into a single jet at approximately 45°S. *Fetter and Matano* [2008] argued that these branches degrade the coherence between the transport variations at the Drake Passage and those in the northern portion of the MC. The main discrepancies between the studies of *Fetter and Matano* [2008] and that of *Piola et al.* [2013] is that while the former reported two jets extending up to 45°S the later reported secondary high-velocity jets extending as far north as 39°S.

The discrepancies between the studies of *Piola et al.* [2013] and *Fetter and Matano* [2008] could be attributed to the limited spatial resolution of the numerical simulations (1/4° resolution), which does not allow representing the small-scale structure of the secondary jets reported in the observations. A better assessment of the multiple jet structure of the MC can be made with the present model. Our experiment shows that, in the mean, the MC south of 45°S is composed of two meridional jets, the weakest one flowing close to the shelf break and the stronger one farther offshore (Figures 18a and 18b). North of 45°S, however, these jets merge, forming a coherent flow that is in agreement with the mean cross-shelf structure reported by
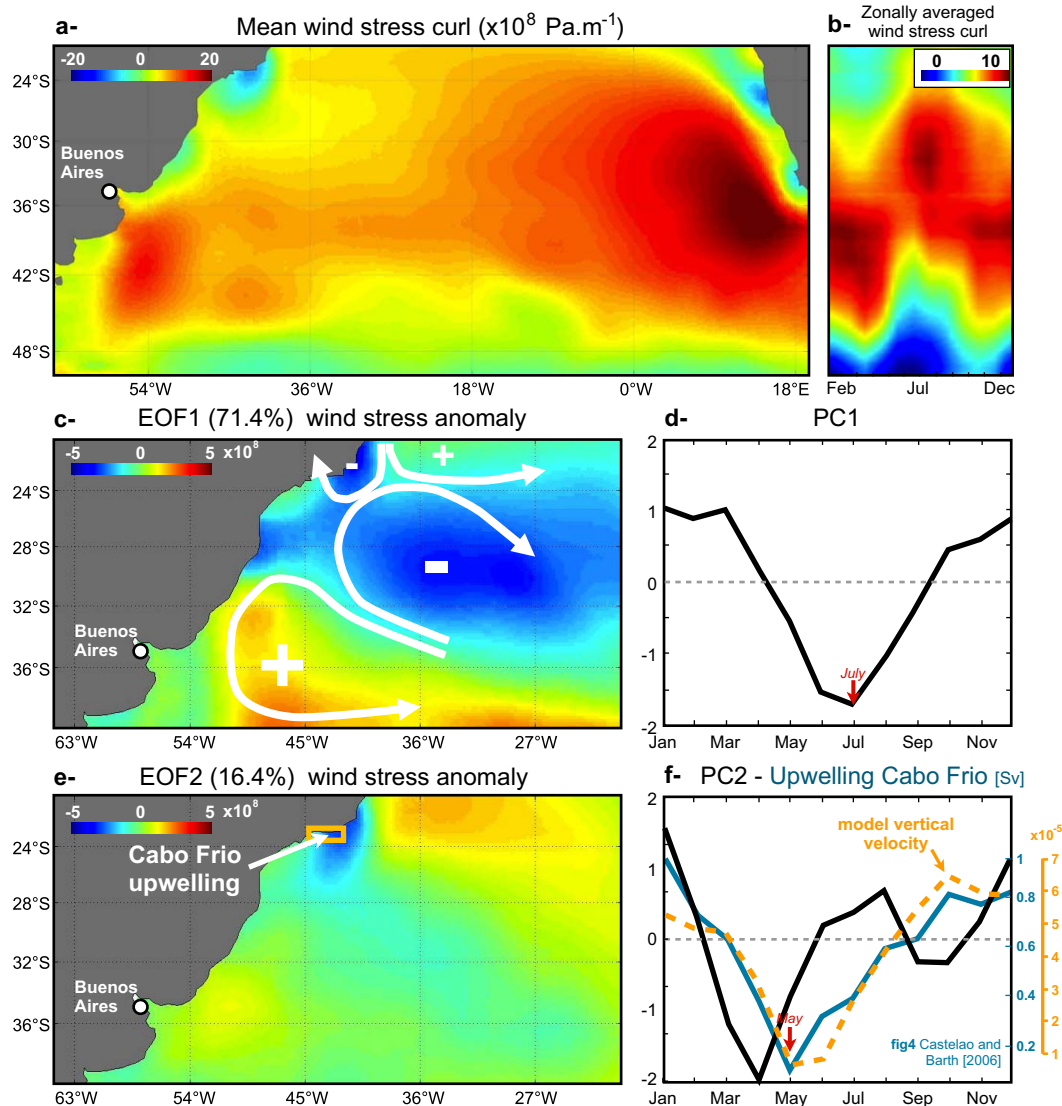
**Figure 15.** (a) Mean and (b) zonally averaged wind stress curl. (c–f) The first and second Empirical Orthogonal Functions (EOF) and Principal Components (PC) of the wind stress curl anomaly (from the mean). Orange line on Figure 15f is the integrated vertical velocity (in m s$^{-1}$) from bottom to surface and averaged over the orange box on Figure 15e. Blue line on Figure 15f is the upwelling index at Cabo Frio, derived from *Castelao and Barth* [2006].

direct, long-term velocity measurements [*Spadone and Provost*, 2009] and with MC velocity structures inferred from drifter data [*Piola et al.*, 2013]. The model results, however, disagrees with the inferences made from satellite-derived mean dynamic topography and snapshots of direct current measurements and hydrographic observations [*Piola et al.*, 2013]. These data sources indicate the existence of discontinuous high-velocity cores in the MC that extend as far north as 39°S. Although our model does not show multiple jets in the mean structure of the MC North of 45°S, multiple jets are regularly observed in snapshots of the alongshelf velocities. Figures 18c and 18d, for example, show three jets south of 45°S and two jets farther north. These multiple jets do not appear in the long-term mean due to the randomness of their occurrence. To further illustrate the development and decay of the multiple jets of the MC, we calculated a Hovmöller diagram of the meridional velocities in a cross-shelf section at 42°S. This diagram demonstrates that the presence of secondary jets in the velocity structure of the MC is a common but highly intermittent phenomenon (Figure 18e). Animations of the model simulation (not shown) indicate that the secondary jets displayed in the Hovmöller diagram are generated by the impact of eddies detached at the BMC, which after being generated are advected toward the southwest by the mean flow and thus reflect the high mesoscale variability of the region (subset on Figure 18c).
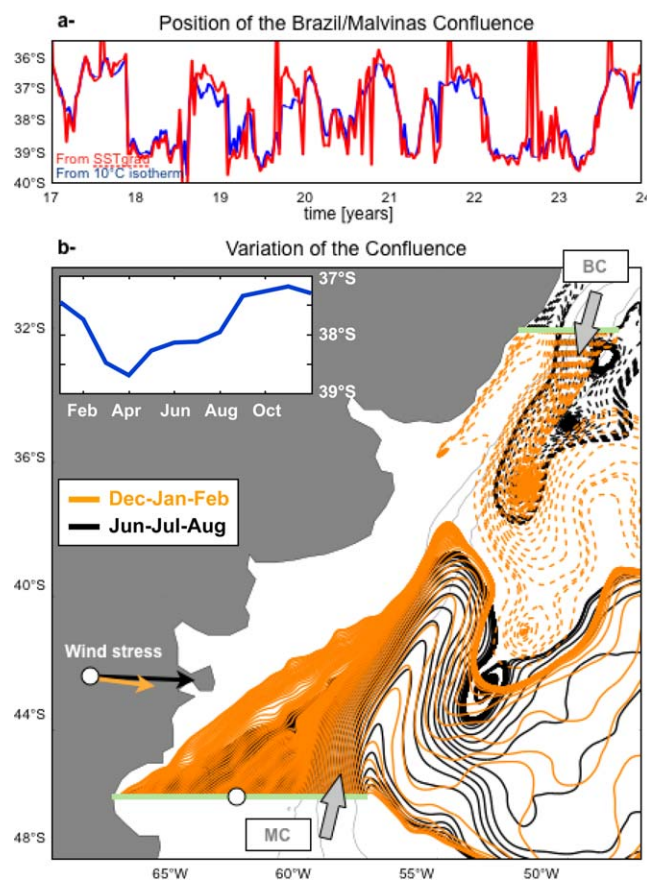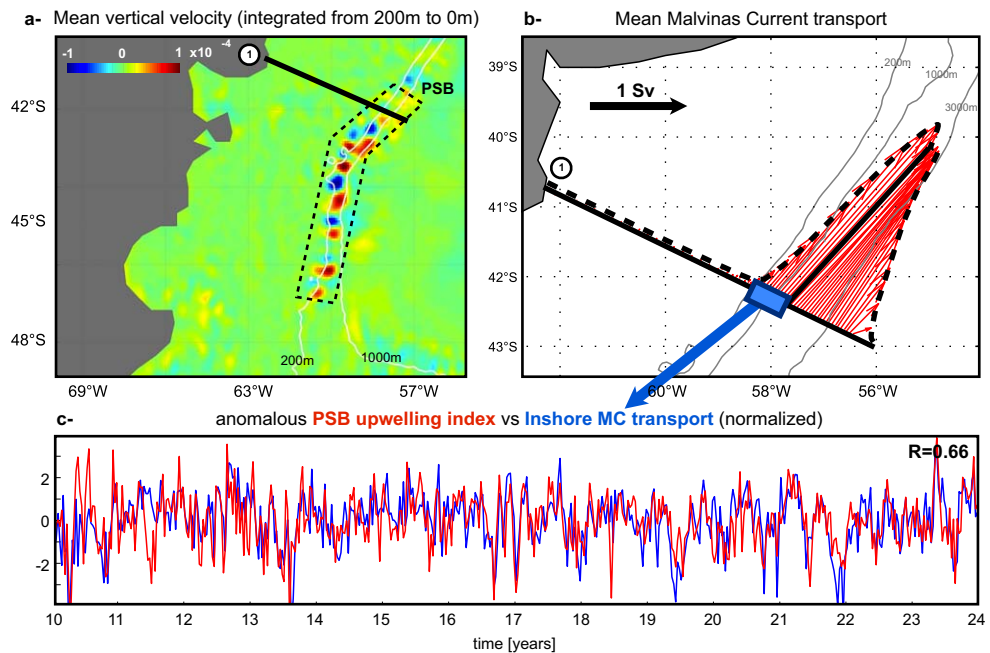
**Figure 16.** (a) Latitude of the separation of the Brazil Current from the continental shelf (blue: defined as the intersection between the 1000 m bathymetry contour and the 10°C contour at 200 m depth; red: defined as the highest SST gradient along the 1000 m isobath). (b) Stream functions of surface currents during austral summer (orange) and winter (black). The stream functions are initialized along the green lines every 0.1° of longitude. The two arrows correspond to the surface wind stress at the white circle (Patagonian shelf) with amplitude of 0.054 N/m² during summer and 0.089 N/m² during winter. The inset shows the seasonal variability of the blue line on Figure 16a.

## 8. Cross-Shelf Exchanges

There is a marked difference between the dynamical processes controlling the cross-shelf exchanges in the northern and southern portion of the southwestern Atlantic shelf. The exchanges over the northern shelf are largely driven by the generation and transit of energetic eddies and meanders of the BC and by bottom boundary layer processes [*Campos et al.*, 2000; *Matano et al.*, 2010]. The cross-shelf exchanges in the southern shelf, however, are controlled by relatively small, steady intrusions of the MC onto the shelf region, on account of the greater stability of this boundary current [*Matano et al.*, 2010]. Although it is well known that the BMC is one of the preferential sites for the detrainment of the shelf waters onto the deep ocean, the role of other portions of the shelf in the cross-shelf exchanges needs to be determined. To assess the exchanges between the shelf and the deep ocean in the southwestern Atlantic region we inject six passive tracers in different regions of the model domain (Figure 19). These tracers are uniformly distributed from the surface to the bottom, and their spatial and temporal evolution is controlled by an advection-diffusion equation that is identical to that used for the temperature and salinity fields.

"Tracer_ACC" is released in a narrow strip in the Drake Passage that extends from the end of South America's shelf to Antarctica. "Tracer_BC" is released off the coast of Southern Brazil (44°W) from the 200 m isobath to 29°S. "Tracer_SS" and "Tracer_NS" are released at the southern and northern Patagonian shelf. "Tracer_LaP" is released at the mouth of the La Plata River. "Tracer_PSB" is released from 46°S to 41.5°S, from the 200 m isobath to the 1000 m isobath. This tracer, which was introduced to track the fate of the subsurface waters in the Patagonian shelf break region, was released in the subsurface layer that extends from 150 m to the bottom. Figures 19a–19c show a snapshot of the surface distribution of the tracers taken 300 days after their initial release.

The final tracer distribution indicates that the entrainment of deep-ocean waters onto the shelf is largely concentrated in the sector between the tip of Tierra del Fuego and the Malvinas Islands (Tracer_ACC), and along the shelf break region north of the BMC (Tracer_BC). The surface Tracer concentration (Figure 19a) shows a surface onshelf advection of sub-Antarctic water (Tracer_ACC), unlike the onshelf intrusion of the Brazil Current water that occurs primarily in the bottom layer (Tracer_BC). The latter onshelf transport is further detailed at the end of the section. The fate of the shelf water is illustrated in Figures 19b and 20. The distribution of Tracer_SS and Tracer_NS indicate that the BMC is the main region for the detrainment of shelf waters onto the deep ocean. Unlike Tracer_SS, Tracer_NS may cross the shelf break outside the BMC

**Figure 17.** (a) The mean vertical velocity integrated from 200 m to the surface. The Patagonian Shelf Break (PSB) upwelling index is defined as the time series of the vertical velocity integrated from 200 to 0 m and averaged over the dashed black box on Figure 17a. (b) The mean Malvinas Current transport at transect 1. (c) Comparison of the anomalous normalized PSB upwelling index (red) and the inshore portion of the MC transport (blue).

under the influence of the more baroclinic BC and its associated mesoscale eddies. To better describe the fate of the shelf water, Figure 20 provides a 3-D view of the Tracer_SS, which to some extent illustrates mechanisms contributing to the fertilization of the deep ocean. As illustrated in Figure 20, Tracer_SS can be found as deep as 1000 m with a clear downwelling at the confluence. The eddy field plays an important role in the transport of shelf water after leaving the Confluence. In particular, warm BC eddies tend to
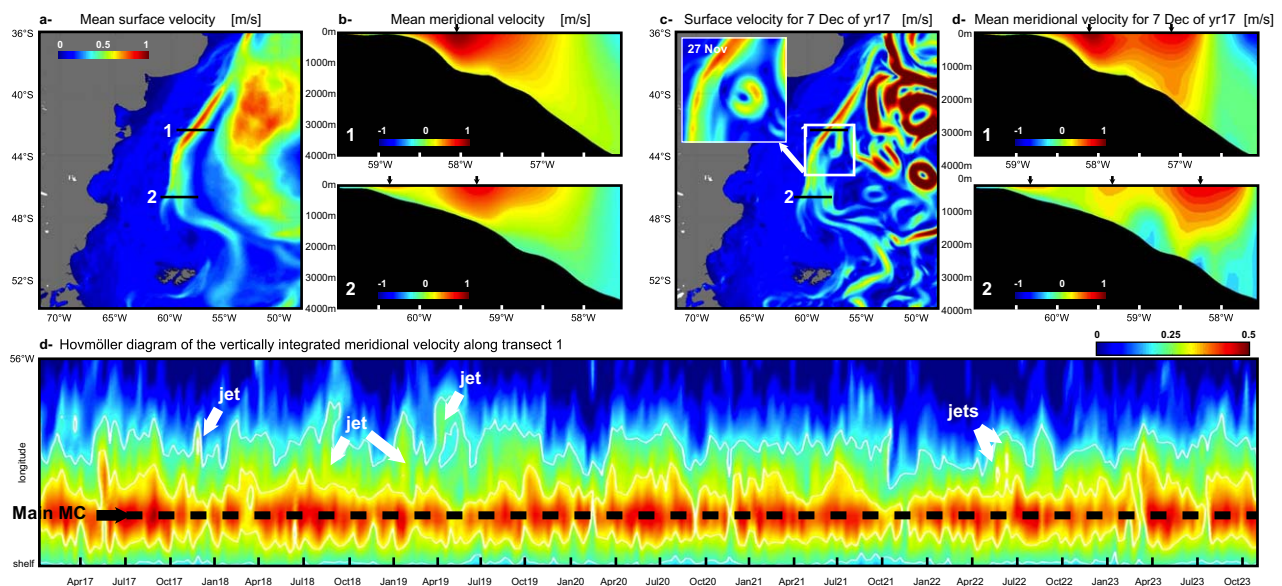


**Figure 18.** Mean (a) Surface velocity [m/s] and (b) meridional velocity [m/s] across Transect 1 and 2. (c and d) Same as Figures 18a and 18b for 7th December of year 17. Subset on Figure 18c shows the surface velocity 10 days prior. (Figure 18d) Hovmöller diagram of the vertically integrated meridional velocity along transect 1. White contours correspond to the 0.2 and 0.3 m/s.
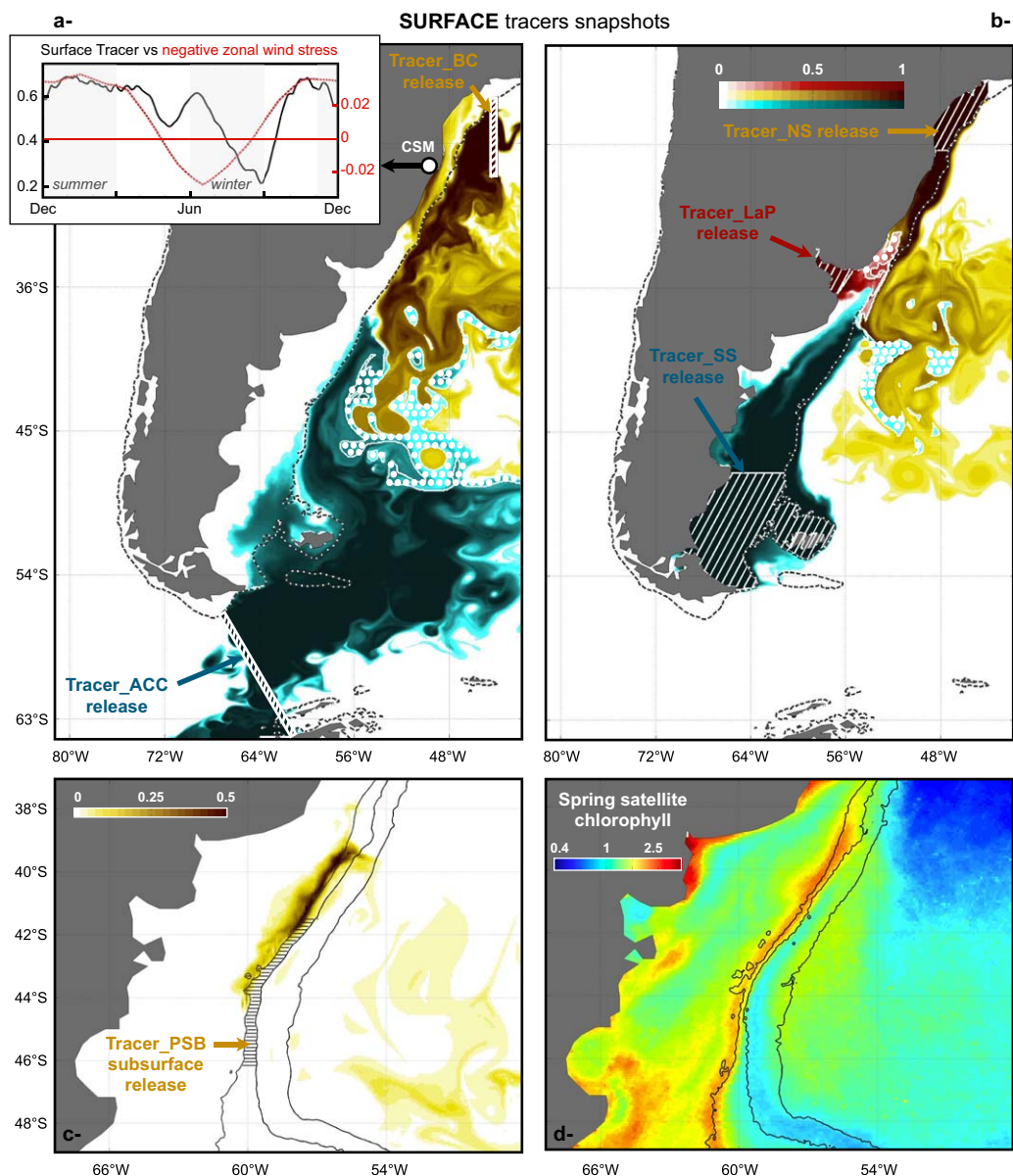
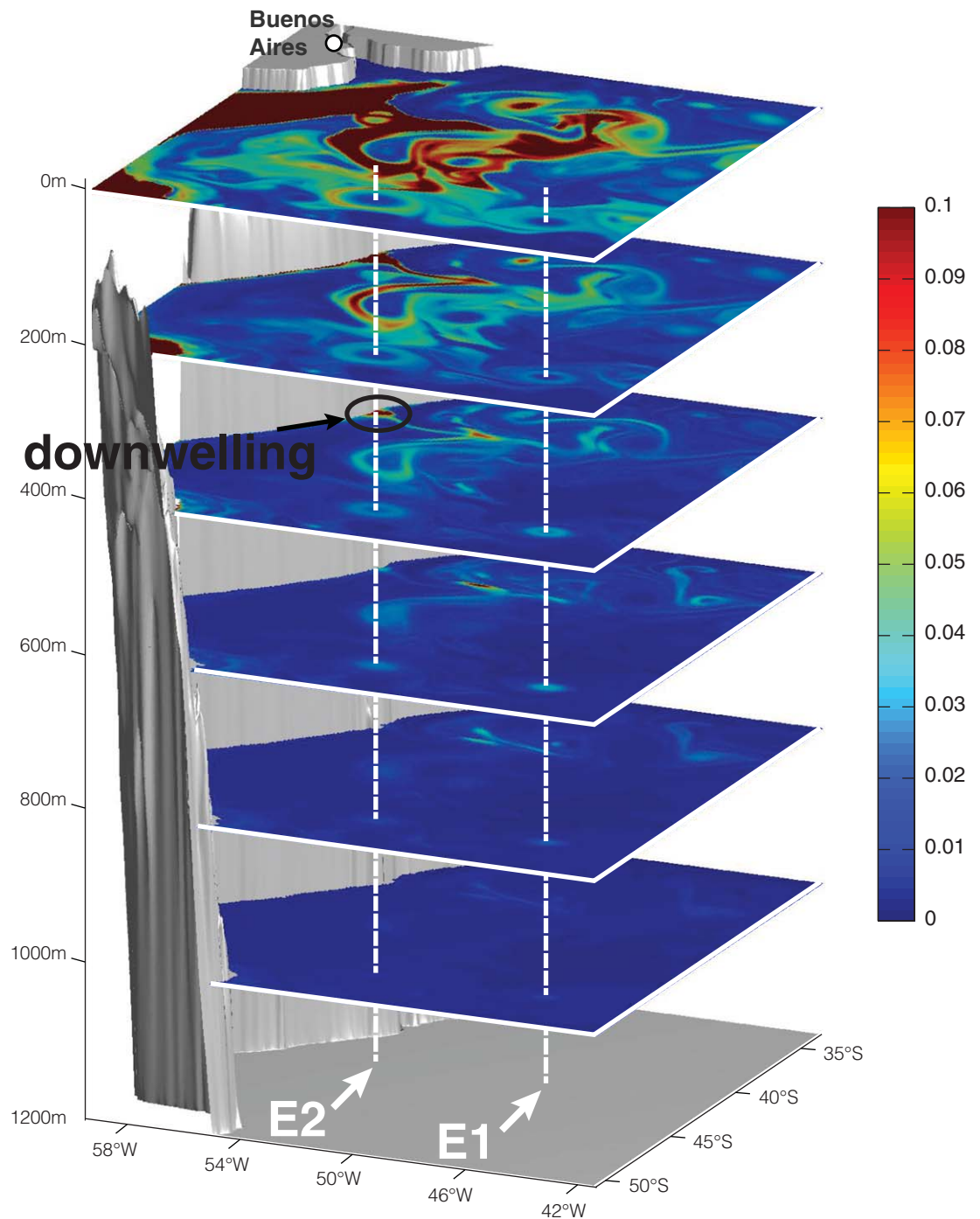**Figure 19.** (a–c) Tracers concentration at the surface after 360 days of model integration. Each tracer is released continuously into the hatched box, from surface to bottom for Tracer_ACC, Tracer_BC, Tracer_SS, Tracer_LaP, Tracer_NS, and below 150 m for Tracer_PSB. (d) The spring satellite chlorophyll from SeaWIFS. The dotted regions on Figures 19a and 19b indicate regions where both tracers concentrations are found Inset figure on Figure 19a shows the surface Tracer_BC (black) and negative zonal wind stress (upwelling favorable wind; red) off the Cape Santa Marta (CSM).

aggregate Tracer_SS in their rim and carry it eastward ("E1," "E2" in Figure 20). The baroclinic structure of those eddies can also be observed in the vertical distribution of Tracer_SS across those eddies. While Tracer_SS is found in the rim of eddies at the surface, below 500 m the tracer is found closer to their core, featuring a dome shape of the tracer concentration. Noteworthy that, the shelf water Tracers are advected around the Zapiola anticyclone.

The surface distribution of Tracer_PSB and Tracer_BC also reveal the different upwelling regimes of the southwestern Atlantic shelf. The shelf break upwelling of Patagonia is evident in the surface distribution of Tracer_PSB, which is characterized by a narrow ribbon of high tracer concentration located on the inshore side of the release location. This pattern corresponds closely with the pattern of chlorophyll-a reported in satellite observations (Figure 19d). In agreement with the satellite chlorophyll observation, we find that

**Figure 20.** Tracer_SS concentration after 360 days model integration at the BMC. "E1" and "E2" indicate two warm core eddies.

while the tracer is released to the east of the shelf break it surfaces west of the shelf break, showing that the upwelling is associated with small onshelf intrusions of the MC as postulated in the upwelling theory of *Matano and Palma* [2008].

Unlike the tracer intrusion in southern Patagonia, which is characterized by a gradient with a maximum in the shelf break and a minimum toward the coast, the onshelf intrusions of Tracer_BC is characterized by a

maximum in the nearshore region and a minimum toward the shelf break (Figure 19a). After its release Tracer_BC is advected poleward by the BC. The portion of the tracer flowing along the shelf break is advected onshore in the bottom boundary layer [*Palma and Matano*, 2009]. After reaching the continental margin of South America the tracer is upwelled by the dominant upwelling winds that characterize this portion of the shelf, whereupon the tracer is advected toward the BMC. Observations indicate that the upwelling regime in this portion of the Brazilian shelf undergoes seasonal variations [*Campos et al*., 2013]. During the austral fall and winter (southwesterly winds) the region is dominated by downwelling favorable winds and the local water mass characteristics are influenced by intrusions of low-salinity waters from the La Plata River. During the austral spring and summer, however, the shelf is under the influence of northeasterly, upwelling favorable, winds that lead to cooler SSTs near the coast. The observed seasonality of the upwelling regime is also confirmed by the variability of the surface Tracer_BC concentration (black line on Figure 19a). The surface Tracer_BC concentration increases at the end of winter when the surface wind stress (dashed red line) shifts from downwelling to upwelling favorable and reaches its maximum concentration during spring and summer. During winter, the coastal circulation reverses from a southward to a northward direction, which replaces the surface water over that region by water originated in the La Plata River. The maximum surface Tracer_BC concentration observed in June on Figure 19a is the northward surface advection of Tracer_BC, which has upwelled previously and advected southward during summer.

## 9. Summary and Conclusions

We discuss the results of a high-resolution, two-way nested simulation of the oceanic circulation in the southwestern Atlantic region. The model results are used to characterize the mean and seasonal variability of the western boundary currents, the upwelling regimes of southern Patagonia, and southern Brazil and to identify the mechanisms driven the interactions between the shelf and deep-ocean circulations. A comparison between the model results and extant observations indicate that the nested model has skill in reproducing the best-known aspects of the regional circulation, e.g., the volume transport of the ACC, the latitudinal position of the BMC, the Patagonian shelf break upwelling, and the Zapiola Anticyclone. Process oriented studies investigate the sensitivity of the location of the BMC, the development of the Zapiola Anticyclone, and the magnitude of the Patagonian shelf break upwelling to the wind stress forcing and the parameterization of bottom friction. Sensitivity experiments indicate that different wind stress data sets produce similar BMC locations because the largest differences between data sets are observed in the southern portion of the Drake Passage rather than the northern portion of the ACC. The northern portion of the ACC is however sensitive to the bottom stress formulation, which significantly modify the location of the BMC. In agreement with previous studies, we also found that the development and strength of the Zapiola Anticyclone is sensitive to the particulars of the bottom friction implementation.

Seasonal variability accounts for ∼9–10% of the total variability of the MC transport. This variability, however, is not uniformly distributed across the MC jet but is concentrated in its offshore portion. The seasonal variations of the BC oppose those of the MC with a strengthening during austral summer and a weakening during austral winter. The seasonal variations of the BC are consistent with the first mode of variability of the wind stress curl over the southwest Atlantic (65°W–20°W, 40°S–20°S). The second mode of variability exhibits a more coastal signature and explains the seasonal variations of the Cabo Frio upwelling. At ∼23°S the Cabo Frio upwelling shows a minimum during May and reaches its maximum strength during the end of austral spring, beginning of summer. Off southeast Brazil between 27°S and 30°S, the model experiment reveals a second local upwelling off the region of Cape Santa Marta. In agreement with *Campos et al*. [2013], the modeled upwelling shows a strong seasonal cycle, with a maximum (minimum) during austral summer (winter) and found to be driven by alongshore wind stress.

Unlike the Cabo Frio and Cape Santa Marta coastal upwellings, the Patagonian shelf break upwelling variability is not driven by surface wind stress. Because the Patagonian shelf break upwelling is on average not uniform along the shelf break (where canyons, changes of bottom slope promote localized upwelling/ downwelling), we constructed a Patagonian shelf break upwelling index, defined as the model vertical velocity averaged from 46°S to 41.5°S and from 200 m to the surface. The theory from *Matano and Palma* [2008] that the effects of bottom friction on the MC should produce a shelf break upwelling is also supported by our modeling experiments. We show that the inshore portion of the MC is highly correlated with

the Patagonian shelf break upwelling index. It is also noteworthy of mentioning that at a smaller time scale, the model also reproduces recent observations from *Piola et al.* [2013] and shows that the mean MC masks its multiple jets structure.

Our numerical simulations also present a method to track the fate of coastal and deep waters as they propagate into the Southwestern Atlantic. The vertical and cross-shelf transports of those water masses have been explored using a passive tracer continuously released across the ACC, into the BC, in the subsurface inshore portion of the MC and over the shelf. We find that while the offshelf transport is mainly concentrated in the BMC, the tracer distributions also reveal onshelf transports from the large-scale BC and MC. For example, the presence of passive tracer at the surface off the Cape Santa Marta confirms the advection of BC originated water into the shelf at the bottom before it upwells at the coast during summer (due to westerly winds). The intrusion of MC water intrusions on the Patagonia continental shelf is also noticed in the distribution of the tracer released in the subsurface across the MC. In particular, we find that the Patagonian shelf break upwelling together with an onshore advection of subsurface MC water bring nutrient-rich deep MC water to the surface water of the shelf region, consistent with the distribution of satellite chlorophyll concentration. It is noteworthy to mention that the impact of Patagonia's shelf break upwelling on the local ecosystem extends beyond the shelf break region. The offshelf advection of high chlorophyll Patagonian shelf break upwelling water through the Confluence and advected far into the deep ocean (captured in chlorophyll images) makes the subpolar portion of the South Atlantic the most productive region of the entire Southern Ocean.

## References

Agra, C., and D. Nof (1993), Collision and separation of boundary currents, *Deep Sea Res., Part I*, *40*(11-12), 2259–2282.

Amante, C., and B. W. Eakins (2009), ETOPO1 1 arc-minute global relief model: Procedures, data sources and analysis, *NOAA Tech. Memor. NESDIS NGDC-24*, 19 pp.

Auad, G., and P. Martos (2012), Climate variability of the northern Argentinean shelf circulation: Impact on engraulis anchoita, *Int. J. Ocean Clim. Syst.*, *3*(1), 17–43.

Barnier, B., et al. (2006), Impact of partial steps and momentum advection schemes in a global ocean circulation model at eddy-permitting resolution, *Ocean Dyn.*, *56*(5–6), 543–567.

Calado, L., I. C. A. daSilveira, A. Gangopadhyay, and B. M. deCastro (2010), Eddy-induced upwelling off Cape São Tomé (22°S, Brazil), *Cont. Shelf Res.*, *30*, 1181–1188, doi:10.1016/j.csr.2010.03.007.

Campos, E. J. D., D. Velhote, and I. C. A. da Silveira (2000), Shelf break upwelling driven by Brazil Current cyclonic Meanders, *Geophys. Res. Lett.*, *27*(6), 751–754.

Campos, P. C., O. O. Moller Jr., A. R. Piola, and E. D. Palma (2013), Seasonal variability and coastal upwelling near Cape Santa Marta (Brazil), *J. Geophys. Res. Oceans*, *118*, 1420–1433, doi:10.1002/jgrc.20131.

Castelao, R. M., and J. A. Barth (2006), Upwelling around Cabo Frio, Brazil: The importance of wind stress curl, *Geophys. Res. Lett.*, *33*, L03602, doi:10.1029/2005GL025182.

Castelao, R. M., E. J. D. Campos, and J. L. Miller (2004), A modelling study of coastal upwelling driven by wind and meanders of the Brazil Current, *J. Coastal Res.*, *20*(3), 662–671.

Cunningham, S. A., S. G. Alderson, B. A. King, and M. A. Brandon (2003), Transport and variability of the Antarctic Circumpolar Current in Drake Passage, *J. Geophys. Res.*, *108*(C5), 8084, doi:10.1029/2001JC001147.

Da Silva, A. M., C. C. Young, and S. Levitus (1994), *Atlas of Surface Marine Data 1994, vol. 1, Algorithms and Procedures*, *NOAA Atlas NESDIS 8*, 83 pp., U. S. Dep. of Commer., NOAA, NESDIS, Washington, D. C.

Da Silveira, I. C. A., L. Calado, B. M. Castro, M. Cirano, J. A. M. Lima, and A. D. S. Mascarenhas (2004), On the baroclinic structure of the Brazil Current–Intermediate Western Boundary Current system at 22°–23°S, *Geophys. Res. Lett.*, *31*, L14308, doi:10.1029/2004GL020036.

De Miranda, A. P., B. Barnier, and W. K. Dewar (1999), On the dynamics of the Zapiola Anticyclone, *J. Geophys. Res.*, *104*(C9), 21,137–21,149.

Debreu, L., P. Marchesiello, P. Penven, and G. Cambon (2011), Two-way nesting in split-explicit ocean models: Algorithms, implementation and validation, *Ocean Modell.*, *49-50*, 1–21.

Dee, D. P., et al. (2011), The ERA-Interim reanalysis: Configuration and performance of the data assimilation system, *Q. J. R. Meteorol. Soc.*, *137*, 553–597, doi:10.1002/qj.828.

Dewar, W. K. (1998), Topography and barotropic transport control by bottom friction, *J. Mar. Res.*, *56*, 295–325.

Egbert, G. D., and S. Y. Erofeeva (2002), Efficient inverse modeling of barotropic ocean tides, *J. Atmos. Oceanic Technol.*, *19*, 183–204.

Fetter, A. F. H., and R. P. Matano (2008), On the origins of the variability of the Malvinas Current in a global, eddy permitting numerical simulation, *J. Geophys. Res.*, *113*, C11018, doi:10.1029/2008JC004875.

Flood, R. D., and A. N. Shor (1998), Mud waves in the Argentine Basin and their relationship to regional bottom circulation patterns, *Deep Sea Res., Part I*, *35*, 943–971.

Franco, B. C., A. R. Piola, A. L. Rivas, A. Baldoni, and J. P. Pisoni (2008), Multiple thermal fronts near the Patagonian shelf break, *Geophys. Res. Lett.*, *35*, L02607, doi:10.1029/2007GL032066.

Garcia, V. M. T., C. A. E. Garcia, M. M. Mata, R. C. Pollery, A. R. Piola, S. R. Signorini, C. R. McClain, and M. D. Iglesias-Rodriguez (2008), Environmental factors controlling the phytoplankton blooms at the Patagonia shelf-break in spring, *Deep Sea Res., Part I*, *55*, 1150–1166.

Garzoli, S. L., and Z. Garraffo, (1989), Transports, frontal motions and eddies at the Brazil-Malvinas Currents Confluence, *Deep-Sea Research*, *36*(5), 681–703.

Glorioso, P. D., and R. A. Flather (1995), A barotropic model of the currents off SE South America, *J. Geophys. Res.*, *100*(C7), 13,427–13,440.

Goni, G. J., and I. Wainer (2001), Investigation of the Brazil Current front variability from altimeter data, *J. Geophys. Res.*, *106*(C12), 31,117–31,128.

Goni, G. J., F. Bringas, and P. N. DiNezio (2011), Observed low frequency variability of the Brazil Current front, *J. Geophys. Res.*, *116*, C10037, doi:10.1029/2011JC007198.

Kalnay, E., et al. (1996), The NCEP/NCAR 40-year reanalysis project, *Bull. Am. Meteorol. Soc.*, *77*, 437–471.

Large, W., J. McWilliams, and S. Doney (1994), Oceanic vertical mixing—A review and a model with a nonlocal boundary-layer parameterization, *Rev. Geophys.*, *32*(4), 363–403.

Lungu, T. (2001), *QuikSCAT Science Data Product User's Manual*, version 2.2, JPL Document D-18053, Jet Propul. Lab., Pasadena, Calif.

Maamaatuaiahutapu, K., V. Garçon, C. Provost, and H. Mercier (1998), Transports of the Brazil and Malvinas Currents at their confluence, *J. Mar. Res.*, *56*, 417–438.

Marchesiello, P., J. C. McWilliams, and A. Shchepetkin (2001), Open boundary conditions for long-term integration of regional oceanic models, *Ocean Modell.*, *3*, 1–20.

Marchesiello, P., L. Debreu, and X. Couvelard (2009), Spurious diapycnal mixing in terrain-following coordinate models: The problem and a solution, *Ocean Modell.*, *26*, 156–169.

Masumoto, Y., et al. (2004), A fifty year eddy-resolving simulation of the World Ocean—Preliminary outcomes of OFES (OGCM for the Earth Simulator), *J. Earth Simulator*, *1*, 31–52.

Matano, R. (1993), On the separation of the Brazil Current from the coast, *J. Phys. Oceanogr.*, *23*, 79–90.

Matano, R. P., and E. D. Palma (2008), On the upwelling of downwelling currents, *J. Phys. Oceanogr.*, *38*, 2482–2500.

Matano, R. P., M. G. Schlax, and D. B. Chelton (1993), Seasonal Variability in the Southwestern Atlantic, *J. Geophys. Res.*, *98*(C10), 18,027–18,035.

Matano, R. P., E. D. Palma, and A. R. Piola (2010), The influence of the Brazil and Malvinas Currents on the Southwestern Atlantic Shelf circulation, *Ocean Sci.*, *6*, 983–995.

Meinen, C. S., A. R. Piola, R. C. Perez, and S. L. Garzoli (2012), Deep Western Boundary Current transport variability in the South Atlantic: Preliminary results from a pilot array at 34.5°S, *Ocean Sci. Discuss.*, *9*, 977–1008.

Mellor, G. L., T. Ezer, and L. Y. Oey (1994), The pressure-gradient conundrum of sigma coordinate ocean models, *J. Atmos. Oceanic Technol.*, *11*, 1126–1134.

Miller, R. L., R. P. Matano, and E. D. Palma (2011), Upwelling induced by alongshelf currents: Analytical and numerical results, *J. Fluid Mech.*, *686*, 239–249. doi:10.1017/jfm.2011.326.

Nowlin, W. D., and J. M. Klinck (1986), The physics of the Antarctic Circumpolar Current, *Rev. Geophys.*, *24*(3), 469–491.

Núñez-Riboni, I., and E. Fahrbach (2009), Seasonal variability of the Antarctic Coastal Current and its driving mechanisms in the Weddell Sea, *Deep Sea Res., Part I*, *56*, 1927–1941, doi:10.1016/j.dsr.2009.06.005.

Olson, D., G. P. Podesta, R. H. Evans, and O. B. Brown (1988), Temporal variations in the separation of Brazil and Malvinas currents, *Deep Sea Res., Part A*, *35*, 1971–1990.

O'Neill, L. W., D. B. Chelton, and S. K. Esbensen (2012), Covariability of surface wind and stress responses to sea surface temperature fronts, *J. Clim.*, *25*, 5916–5942.

Orsi, A. H., T. Whitworth, and W. D. Nowlin (1995), On the meridional extent and fronts of the Antarctic Circumpolar Current, *Deep Sea Res., Part I*, *42*(5), 64–673.

Painter, S. C., A. J. Poulton, J. T. Allen, R. Pidcock, and W. M. Balch (2010), The COPAS'08 expedition to the Patagonian Shelf: Physical and environmental conditions during the 2008 coccolithophore bloom, *Cont. Shelf Res.*, *30*, 1907–1923.

Palma, E. D., and R. P. Matano (2009), Disentangling the upwelling mechanisms of the South Brazil Bight, *Cont. Shelf Res.*, *29*, 1525–1534.

Palma, E. D., R. P. Matano, and A. R. Piola (2004), A numerical study of the Southwestern Atlantic Shelf circulation: Barotropic response to tidal and wind forcing, *J. Geophys. Res.*, *109*, C08014, doi:10.1029/2004JC002315.

Palma, E. D., R. P. Matano, and A. R. Piola (2008), A numerical study of the Southwestern Atlantic Shelf circulation: Stratified ocean response to local and offshore forcing, *J. Geophys. Res.*, *113*, C11010, doi:10.1029/2007JC004720.

Penduff, T., B. Barnier, K. Béranger, and J. Verron (2001), Comparison of near-surface mean and eddy flows from two numerical models of the South Atlantic Ocean, *J. Geophys. Res.*, *106*(C8), 16,857–16,867.

Penven, P., P. Marchesiello, L. Debreu, and J. Lefevre (2008), Software tools for pre- and post-processing of oceanic regional simulations, *Environ. Modell. Software*, *23*, 660–662, doi:1016/j.envsoft.2007.07.004.

Peterson, R. G., and L. Stramma (1991), Upper-level circulation in the South Atlantic Ocean, *Prog. Oceanogr.*, *26*, 1–73.

Piola, A. R., E. J. Campos, O. Möller Jr., M. Charo, and C. Martinez (2000), Subtropical shelf front off eastern South America, *J. Geophys. Res.*, *105*(C3), 6565–6578.

Piola, A. R., S. I. Romero, and U. Zajaczkovski (2008), Space–time variability of the Plata plume inferred from ocean color, *Cont. Shelf Res.*, *28*, 1556–1567.

Piola, A. R., B. C. Franco, E. D. Palma, and M. Saraceno (2013), Multiple jets in the Malvinas Current, *J. Geophys. Res. Oceans*, *118*, 2107–2117, doi:10.1002/jgrc.20170.

Romero, S. I., A. R. Piola, M. Charo, and C. A. Eiras Garcia (2006), Chlorophyll-a variability off Patagonia based on SeaWiFS data, *J. Geophys. Res.*, *111*, C05021, doi:10.1029/2005JC003244.

Saraceno, M., C. Provost, A. R. Piola, J. Bava, and A. Gagliardini (2004), Brazil Malvinas Frontal System as seen from 9 years of advanced very high resolution radiometer data, *J. Geophys. Res.*, *109*, C05027, doi:10.1029/2003JC002127.

Saraceno, M., C. Provost, and A. R. Piola (2005), On the relationship between satellite-retrieved surface temperature fronts and chlorophyll a in the western South Atlantic, *J. Geophys. Res.*, *110*, C11016, doi:10.1029/2004JC002736.

Sasaki, H., Y. Sasai, S. Kawahara, M. Furuichi, F. Araki, A. Ishida, Y. Yamanaka, Y. Masumoto, and H. Sakuma (2004), A Series of Eddy-resolving Ocean Simulations in the World Ocean: OFES (OGCM for the Earth Simulator) Project, *OCEAN'04*, *3*, 1535–1541.

Sasaki, H., M. Nonaka, Y. Masumoto, Y. Sasai, H. Uehara, and H. Sakuma (2008), An eddy-resolving hindcast simulation of the quasi-global ocean from 1950 to 2003 on the Earth Simulator, in *High Resolution Numerical Modelling of the Atmosphere and Ocean*, edited by K. Hamilton and W. Ohfuchi, pp. 157–185, Springer, New York.

Sassi, M. G., and E. D. Palma (2006), Modelo hidrodinamico del estrecho de Magallanes, *Mec. Comput.*, *XXV*, 1461–1477.

Saunders, P. M., and B. A. King (1995), Bottom currents derived from a Shipborne ADCP on the WOCE Cruise A11 in the South Atlantic, *J. Phys. Oceanogr.*, *25*, 329–347.

Shchepetkin, A., and J. C. McWilliams (2005), The regional oceanic modeling system (ROMS): A split explicit, free-surface, topography-following-coordinate oceanic model, *Ocean Modell.*, *9*, 347–404.

Smith, L. T., E. P. Chassignet, and D. B. Olson (1994), Wind-forced variations in the Brazil-Malvinas Confluence region as simulated in a coarse resolution numerical model of the South Atlantic, *J. Geophys. Res.*, *99*(C3), 5095–5117.

Spadone, A., and C. Provost (2009), Variations in the Malvinas Current volume transport since October 1992, *J. Geophys. Res.*, *114*, C02002, doi:10.1029/2008JC004882.

Tchernia, P. (1981), Observation of the Antarctic East Wind Drift Current by using tabular icebergs tracked by satellite, *Antarct. J. U. S.*, *15*, 83.

Tchernia, P., and P. F. Jeannin (1980), Observations on the Antarctic East Wind Drift using tabular icebergs tracked by satellite Nimbus F (1975–1977), *Deep Sea Res., Part A*, *27*, 467–474.

Tokinaga, H., Y. Tanimoto, and S. P. Xie (2005), SST-induced surface wind variations over the Brazil-Malvinas confluence: Satellite and in situ observations, *J. Clim.*, *18*(17), 3470–3482, doi:10.1175/JCLI3485.1.

Treguier, A. M., B. Barnier, A. P. de Miranda, J. M. Molines, N. Grima, M. Imbard, G. Madec, C. Messager,T. Reynaud, and S. Michel (2001), An eddy-permitting model of the Atlantic circulation: Evaluating open boundary conditions, *J. Geophys. Res.*, *106*(C10), 22,115–22,129.

Vivier, F., and C. Provost (1999), Volume transport of the Malvinas Current: Can the flow be monitored by TOPEX/Poseidon?, *J. Geophys. Res.*, *104*(C9), 21,105–21,122, doi:10.1029/1999JC900056.

Wainer, I., P. Gent, and G. Goni (2000), Annual cycle of the Brazil-Malvinas confluence region in the National Center for Atmospheric Research Climate System Model, *J. Geophys. Res.*, *105*(C11), 26,167–26,177.

Whitworth, T., III, and R. G. Peterson (1985), Volume transport of the Antarctic Circumpolar Current from bottom pressure measurements, *J. Phys. Oceanogr.*, *15*(6), 810–816.